Micropolar Crystal Plasticity

J.R. Mayeur, D.L. McDowell, and S. Forest

Contents

J.R. Mayeur
Theoretical Division, Los Alamos National Laboratory, Los Alamos, NM, USA
e-mail: jason.mayeur@gmail.com

D.L. McDowell
Woodruff School of Mechanical Engineering, School of Materials Science and Engineering,
Georgia Institute of Technology, Atlanta, GA, USA
e-mail: david.mcdowell@me.gatech.edu

S. Forest (✉)
Centre des Matériaux UMR 7633, Mines ParisTech CNRS, Evry, France
e-mail: samuel.forest@mines-paristech.fr

Abstract

This chapter considers advances over the past 15 years achieved by the authors and coworkers on generalized crystal plasticity to address size and configuration effects in dislocation plasticity at the micron scale. The specific approaches addressed here focus on micropolar and micromorphic theories rather than adopting strain gradient theory as the starting point, as motivated by the pioneering ideas of Eringen (Eringen and Suhubi 1964; Eringen and Claus Jr 1969; Eringen 1999). It is demonstrated with examples that for isotropic elasticity and specific sets of slip systems, a dislocation-based formulation of micropolar or micromorphic type provides results comparable to discrete dislocation dynamics and has much in common with the structure of Gurtin's slip gradient theory (Gurtin 2002; Gurtin et al. 2007).

Introduction

The collective behavior of dislocations in a single crystal can be described by means of the continuum theory of dislocations. The material volume element is assumed to contain a suitable density of dislocations for the continuum theory of dislocations to be applicable. Nonhomogeneous plastic deformations induce material and lattice incompatibilities that are resolved by a suitable distribution of the dislocation density tensor field which can be interpreted as a second rank statistical mean for a population of arbitrary dislocations inside a material volume element (Kröner 1969; Cermelli and Gurtin 2001). Nye's fundamental relation linearly connects the dislocation density tensor to the lattice curvature field of the crystal. This fact has prompted many authors to treat a continuously dislocated crystal as a Cosserat continuum (Günther 1958; Kröner 1963; Schäfer 1969; Forest et al. 2000). The Cosserat approach records only the lattice curvature of the crystal but neglects the effect of the rotational part of the elastic strain tensor, which is a part of the total dislocation density tensor (Cordero et al. 2010). Full account of plastic incompatibility is taken in strain gradient plasticity theories, starting from the original work by Aifantis (1984) up to the work of Gurtin (2002). Formulation of crystal plasticity within the micromorphic framework is more recent and was suggested by Clayton et al. (2005) for a large spectrum of crystal defects, including point defects and disclinations. Limiting the discussion to dislocation density tensor effects, also called geometrically necessary dislocation (GND) effects, Cordero et al. (2010) showed, within a small deformation setting, how the micromorphic model can be used to predict grain and precipitate size effects in laminate crystalline materials. In particular, the micromorphic model is shown to deliver more general scaling laws than conventional strain gradient plasticity. These models represent extensions of the conventional crystal plasticity theory (cf. Teodosiu and Sidoroff

1976) that accounts for single crystal hardening and lattice rotation but does not incorporate the effect of the dislocation density tensor.

The layout of the chapter is as follows. Classical single crystal plasticity theory is first recalled in section "Finite Deformation Kinematics" including the thermodynamical framework and the definition of the continuum dislocation density tensor. The Cosserat generalization of crystal plasticity is presented in section "Micropolar Single Crystal Plasticity" with its relation to strain gradient plasticity. The section "Applications: Comparison to 2D Discrete Dislocation Dynamics Simulations" provides applications including a comparison between Cosserat constitutive laws and results from discrete dislocation dynamics in the case of constrained thin films in shear and bending.

Classical Single Crystal Plasticity

Finite Deformation Kinematics

The classical theory of finite deformation single crystal plasticity is based on a multiplicative decomposition of the deformation gradient into elastic and plastic parts,

$$\mathbf{F} = \mathbf{F}^e \mathbf{F}^p \tag{1}$$

where $\mathbf{F}^p$ describes the plastic deformation of the continuum that leaves the underlying lattice vectors unaltered and $\mathbf{F}^e$ describes the elastic stretching and rotation of the lattice relative to this intermediate, isoclinic configuration. The deformation gradient maps infinitesimal vectors from the reference to current configuration and can be expressed in terms of the referential gradient of the displacement field as

$$d\mathbf{x} = \mathbf{F} d\mathbf{X}, \quad \mathbf{F} = \mathbf{1} + \mathbf{H}, \quad \mathbf{H} = \mathbf{u} \nabla_0 \tag{2}$$

$\mathbf{H}$ is the distortion (or displacement gradient) tensor and has been introduced for use in subsequent sections. The theory is completed by supplying constitutive prescriptions for the relationships between $\mathbf{F}^e$ and the Cauchy stress and to provide an evolution equation for $\mathbf{F}^p$ (and any associated internal state variables) consistent with thermodynamics.

Thermodynamics

The standard nonpolar mechanical balance laws (neglecting inertial terms) are given in the current configuration as

$$\boldsymbol{\sigma} \cdot \nabla + \mathbf{f} = \mathbf{0}, \quad \boldsymbol{\sigma} = \boldsymbol{\sigma}^T \tag{3}$$

with the associated traction boundary condition, $\mathbf{t} = \boldsymbol{\sigma}\mathbf{n}$, where $\boldsymbol{\sigma}$ is the Cauchy stress tensor, $\mathbf{f}$ is a body force vector, $\mathbf{t}$ is the traction vector, and $\mathbf{n}$ is the unit normal to the external part of the boundary where tractions are specified. The total energy balance can be expressed as

$$\rho\dot{U} = \boldsymbol{\sigma} : \mathbf{D} - \nabla \cdot \mathbf{q} \tag{4}$$

where ρ is the current density, U is the specific internal energy, $\mathbf{D}$ is the rate of deformation tensor, and $\mathbf{q}$ is the heat flux vector. The entropy inequality which will be used to derive the state equations and guide the construction of plastic evolution equations is given as

$$\rho\dot{\eta} + \nabla \cdot \left(\frac{\mathbf{q}}{T}\right) \geq 0 \tag{5}$$

where η is the specific entropy, and T is temperature. Using the state relation $\psi = U - T\eta$, Eqs. (4) and (5) can be combined to obtain the Clausius-Duhem inequality

$$\boldsymbol{\sigma} : \mathbf{D} - \rho\left(\dot{\psi} + \dot{T}\eta\right) - \frac{1}{T}\mathbf{q} \cdot \nabla T \geq 0 \tag{6}$$

where the intrinsic (Δ^{intr}) and thermal (Δ^{th}) dissipation are defined as

$$\Delta^{intr} = \boldsymbol{\sigma} : \mathbf{D} - \rho\left(\dot{\psi} + \dot{T}\eta\right), \quad \Delta^{th} - \frac{1}{T}\mathbf{q} \cdot \nabla T \tag{7}$$

Next, we derive an expression for the stress power in the intermediate configuration by using the relationship between the Cauchy stress and the second Piola-Kirchhoff stress with respect to the intermediate configuration $\tilde{\mathbf{S}} = J^e\mathbf{F}^{e-1}\boldsymbol{\sigma}\mathbf{F}^{e-T}$ and by writing the velocity gradient in terms of the multiplicative decomposition, i.e.,

$$\mathbf{L} = \dot{\mathbf{F}}\mathbf{F}^{-1} = \dot{\mathbf{F}}^e\mathbf{F}^{e-1} + \mathbf{F}^e\dot{\mathbf{F}}^p\mathbf{F}^{p-1}\mathbf{F}^{e-1} \tag{8}$$

such that

$$\frac{1}{\rho}\boldsymbol{\sigma} : \mathbf{L} = \frac{1}{\tilde{\rho}}\left(\tilde{\mathbf{S}} : \dot{\tilde{\mathbf{E}}}^e + \boldsymbol{\Pi}^M : \tilde{\mathbf{L}}^p\right) \tag{9}$$

where $\tilde{\rho}$ is the density in the intermediate configuration, $\tilde{\mathbf{E}}^e$ is the elastic Green-Lagrange strain, $\boldsymbol{\Pi}^M$ is the Mandel stress tensor, and $\tilde{\mathbf{L}}^p$ is the plastic velocity gradient in the intermediate configuration which have the following definitions

$$\tilde{\mathbf{E}}^e = \frac{1}{2}\left(\mathbf{F}^{eT}\mathbf{F}^e - \mathbf{1}\right), \quad \boldsymbol{\Pi}^M = \mathbf{F}^{eT}\mathbf{F}^e\tilde{\mathbf{S}}, \quad \tilde{\mathbf{L}}^p = \dot{\mathbf{F}}^p\mathbf{F}^{p-1}. \tag{10}$$

Equation (9) identifies the appropriate power-conjugate variables in the intermediate configuration, from which it can be seen that $\tilde{\mathbf{E}}^e$ is the strain measure power-conjugate to $\tilde{\mathbf{\Pi}}^e$ and that $\mathbf{\Pi}^M$ is power-conjugate to $\tilde{\mathbf{L}}^p$. If we now introduce the Helmholtz free energy, $\psi = \hat{\psi}\left(\tilde{\mathbf{E}}^e, T, \zeta^\alpha\right)$, the following expression is obtained by inserting the right-hand side of Eq. (9) along with the chain rule expression of the time derivative of ψ into the Clausius-Duhem inequality

$$\left(\mathbf{\Pi}^e - \tilde{\rho}\frac{\partial\psi}{\partial\tilde{\mathbf{E}}^e}\right) : \dot{\tilde{\mathbf{E}}}^e - \tilde{\rho}\left(\eta + \frac{\partial\psi}{\partial T}\right)\dot{T} + \mathbf{\Pi}^M : \tilde{\mathbf{L}}^p - \tilde{\rho}\sum_\alpha \frac{\partial\psi}{\partial\zeta^\alpha} * \dot{\zeta}^\alpha \geq 0. \quad (11)$$

where ζ^α is a set of internal state variables. Here, "$*$" is an appropriate scalar product operator for the rank of tensor ζ^α. The state laws are then deduced as

$$\mathbf{\Pi}^e = \tilde{\rho}\frac{\partial\psi}{\partial\tilde{\mathbf{E}}^e}, \quad \eta = -\frac{\partial\psi}{\partial T}. \quad (12)$$

and the residual intrinsic dissipation is then expressed as

$$\Delta^{intr} = \mathbf{\Pi}^M : \tilde{\mathbf{L}}^p - \sum_\alpha r^\alpha * \dot{\zeta}^\alpha \geq 0, \quad r^\alpha = \tilde{\rho}\frac{\partial\psi}{\partial\zeta^\alpha}. \quad (13)$$

Therefore, thermodynamically consistent evolution equations for $\tilde{\mathbf{L}}^p$ and $\dot{\zeta}^\alpha$ may be derived by introducing a convex dissipation potential $\Omega = \hat{\Omega}\left(\mathbf{\Pi}^M, r^\alpha\right)$ such that

$$\tilde{\mathbf{L}}^p = \frac{\partial\Omega}{\partial\mathbf{\Pi}^M}, \quad \dot{\zeta}^\alpha = -\frac{\partial\Omega}{\partial r^\alpha} \quad (14)$$

Representative functional forms for $\hat{\psi}$ and $\hat{\Omega}$ are given for completeness below. It is typical to use a free energy that is quadratic with respect to its arguments, i.e.,

$$\tilde{\rho}\psi\left(\tilde{\mathbf{E}}^e, \zeta^\alpha\right) = \frac{1}{2}\tilde{\mathbf{E}}^e : \tilde{\mathbb{C}} : \tilde{\mathbf{E}}^e + \frac{1}{2}\sum_{\alpha,\beta} a^{\alpha\beta}\zeta^\alpha\zeta^\beta \quad (15)$$

where $\tilde{\mathbb{C}}$ is the fourth-order elasticity tensor in the intermediate configuration and $a^{\alpha\beta}$ is positive definite interaction matrix that describes the coupling between the ζ^α. Likewise, a typical power law potential for the inelastic evolution equations is given as

$$\Omega\left(\mathbf{\Pi}^M, r^\alpha\right) = \frac{\dot{\gamma}_0}{n+1}\sum_\alpha g^\alpha\left\langle\frac{\mathcal{F}^\alpha}{g^\alpha}\right\rangle^{n+1} \quad (16)$$

where n is the power law exponent, g^α is viscous stress, $\dot{\gamma}_0$ a typical strain rate parameter, and $\mathcal{F}^\alpha$ is a yield function. The brackets $\langle\bullet\rangle = \text{Max}(\bullet, 0)$ have been

introduced. The yield function is defined in terms of the resolved shear stress, τ^α, and the energetic flow resistance, r^α, as

$$\mathcal{F}^\alpha = \tau^\alpha - (r_0 + r^\alpha), \ \tau^\alpha = \mathbf{\Pi}^M : (\tilde{\mathbf{s}}^\alpha \otimes \tilde{\mathbf{n}}^\alpha) \tag{17}$$

The slip direction vector and the normal to the slip plane for slip system α are respectively denoted by $\tilde{\mathbf{s}}^\alpha$ and $\tilde{\mathbf{n}}^\alpha$ in the undistorted lattice configuration.

Deformation Incompatibility and the GND Density Tensor

Finite Deformation Kinematics

For a classical Cauchy continuum, compatibility of the displacement field requires that the curl of the deformation gradient vanishes, i.e.,

$$\oint_c d\mathbf{x} = \oint_C \mathbf{F} d\mathbf{X} = \mathbf{0} \Rightarrow \mathbf{F} \times \nabla_0 = \mathbf{0} \tag{18}$$

During an inhomogeneous elastic-plastic deformation, the elastic and plastic deformation maps are not compatible and can be used to quantify the heterogeneity of the deformation field in terms of the net Burgers on the intermediate configuration, i.e.,

$$\tilde{\mathbf{b}} = \oint_{\tilde{c}} d\tilde{\mathbf{x}} = \oint_c \mathbf{F}^{e-1} d\mathbf{x} = \oint_C \mathbf{F}^p d\mathbf{X} \tag{19}$$

Making use of Stokes' theorem, the last two expressions in Eq. (19) can be expressed in terms of surface integrals as

$$\tilde{\mathbf{b}} = \int_s \mathbf{A}^e \mathbf{n} da = \oint_S \mathbf{A}^p \mathbf{N} dA \tag{20}$$

where $\mathbf{A}^e = \mathbf{F}^{e-1} \times \nabla$ and $\mathbf{A}^p = \mathbf{F}^p \times \nabla_0$ are the corresponding two-point geometrically necessary dislocation density tensors that map from current to intermediate and reference to intermediate configurations, respectively.

There have been many works in the last two decades focused on incorporating the effects of GNDs into crystal plasticity modeling frameworks. It is beyond the scope of this chapter to attempt to review the myriad ways in which these extensions are carried out. The vast majority of generalized crystal plasticity models that incorporate the effects of GNDs do so by computing them from the plastic slip gradients (so-called slip gradient theories) rather than via gradients of $\mathbf{F}^{e-1}$. While the connection between slip gradients and GND densities can be established in a finite deformation context (see Kuroda and Tvergaard 2008), in this section, the presentation is limited to the linearized kinematic setting for ease of presentation

and direct connection with the pioneering work of Nye (1953). The subsequent developments closely follow the presentation of Arsenlis and Parks (1999).

Linearized Kinematics

In the case of linearized kinematics, the multiplicative decomposition of the deformation gradient is replaced with an additive decomposition of the distortion tensor, i.e., $\mathbf{H} = \mathbf{H}^e + \mathbf{H}^p$ and Eq. (18) may conveniently be rewritten as

$$\mathbf{H} \times \nabla = 0 \tag{21}$$

The continuum GND density tensor, $\mathbf{A} \approx \mathbf{A}^e \approx \mathbf{A}^p$, can be equivalently expressed in terms of either the elastic or plastic distortion as

$$\mathbf{A} = -\mathbf{H}^e \times \nabla = \mathbf{H}^p \times \nabla \tag{22}$$

The lattice torsion-curvature is defined as the gradient of the lattice rotation vector (Nye 1953), i.e.,

$$\boldsymbol{\kappa} = \boldsymbol{\phi}\nabla \tag{23}$$

where ϕ is given by

$$\phi = -\frac{1}{2}\boldsymbol{\epsilon} : \ \text{skw}(\mathbf{H}^e) \tag{24}$$

where "skw" is the skew operator providing the antisymmetric part of the tensor. The notation $\boldsymbol{\epsilon}$ is used for the permutation tensor. Combining Eqs. (22), (23), and (24) the lattice torsion-curvature may be expressed as

$$\varkappa = \underbrace{-\mathbf{A}^{\mathrm{T}} + \frac{1}{2}\text{tr}(\mathbf{A})\,\mathbf{1}}_{\text{Nye curvature},\,\kappa} - (\varepsilon^e \times \nabla)^{\mathrm{T}} \tag{25}$$

where ε^e is the elastic strain tensor which is symmetric. As indicated in Eq. (25), the first two terms represent Nye's original torsion-curvature tensor since it was assumed that $\mathbf{H}^e \approx \text{skw}(\mathbf{H}^e)$.

Next, we seek an expression for $\mathbf{A}$ in terms of slip gradients which can be obtained from taking the curl of the plastic distortion. First, note that the discrete version of Nye's tensor, $\mathbf{A}^d$, for a population of straight edge and screw dislocations can be written as

$$\mathbf{A}^d = b \sum_\alpha \underbrace{\left(\varrho_\perp^\alpha - \varrho_\top^\alpha\right)}_{\varrho_{G\perp}^\alpha} \mathbf{s}^\alpha \otimes \mathbf{t}^\alpha + \underbrace{\left(\varrho_\odot^\alpha - \varrho_\otimes^\alpha\right)}_{\varrho_{G\odot}^\alpha}\mathbf{s}^\alpha \otimes \mathbf{s}^\alpha \tag{26}$$

where $\varrho_\perp^\alpha$ is the positive edge dislocation density, $\varrho_\top^\alpha$ is the negative edge dislocation density, $\varrho_\odot^\alpha$ is the positive screw dislocation density, $\varrho_\otimes^\alpha$ is the negative screw dislocation density, $\varrho_{G\perp}^\alpha$ is the edge GND density, and $\varrho_{G\odot}^\alpha$ is the screw GND density. The continuous expression of Nye's GND density tensor is then obtained as

$$
\begin{aligned}
\mathbf{A} &= \mathbf{H}^p \times \nabla \\
&= \sum_\alpha \gamma^\alpha \mathbf{s}^\alpha \otimes \mathbf{n}^\alpha \times \nabla \\
&= \sum_\alpha \left(-\nabla\gamma^\alpha \cdot \mathbf{s}^\alpha \right) \mathbf{s}^\alpha \otimes \mathbf{t}^\alpha + \left(\nabla\gamma^\alpha \cdot \mathbf{t}^\alpha \right) \mathbf{s}^\alpha \otimes \mathbf{s}^\alpha
\end{aligned}
\tag{27}
$$

Comparing these two expressions for Nye's tensor, it may be shown that the continuum GND densities are given by slip gradients projected in the glide directions for the respective dislocation populations, i.e.,

$$
\varrho_{G\perp}^\alpha = -b^{-1}\nabla\gamma^\alpha \cdot \mathbf{s}^\alpha, \quad \varrho_{G\odot}^\alpha = b^{-1}\nabla\gamma^\alpha \cdot \mathbf{t}^\alpha
\tag{28}
$$

An expression relating Nye's torsion-curvature tensor, κ, to the GND densities is obtained by inserting Eq. (27) into the first two terms in Eq. (25)

$$
\kappa = -b \sum_\alpha \left[\varrho_{G\perp}^\alpha \mathbf{t}^\alpha \otimes \mathbf{s}^\alpha + \varrho_{G\odot}^\alpha \left(\mathbf{s}^\alpha \otimes \mathbf{s}^\alpha - \frac{1}{2}\mathbf{1} \right) \right]
\tag{29}
$$

We will revisit the expression given in Eq. (29) when motivating constitutive equations in subsequent sections.

Micropolar Single Crystal Plasticity

Finite Deformation Theory

The presentation is given here within the finite deformation framework before returning to the linearized case.

Kinematics

A micropolar continuum is a generalized continua with extra rotational degrees of freedom. Considering two sets of vector triads attached to each material point in the reference configuration, $\mathbf{X}$, there is an independent mapping of the two sets of vectors to the current configuration such that

$$
d\mathbf{x}_i = \mathbf{F}d\mathbf{X}_i, \quad \mathbf{d}_i = \overline{\mathbf{R}}\mathbf{D}_i \quad \forall i = 1, 3
\tag{30}
$$

where $\mathbf{F}$ is the usual deformation gradient (see Eq. (2)) and $\overline{\mathbf{R}}$ is the two-point tensor that maps the microstructure triad in the reference configuration, $\mathbf{D}_i$ to its image in

the current configuration, $\mathbf{d}_i$. $\overline{\mathbf{R}}$ is the micropolar rotation tensor; the overbar is used to distinguish it from the rotational part of the deformation gradient obtained via the polar decomposition, i.e., $\mathbf{F} = \mathbf{R}\mathbf{U}$. The micropolar rotation tensor is a proper orthogonal tensor such that the following relations hold:

$$\overline{\mathbf{R}}\,\overline{\mathbf{R}}^T = \mathbf{1}, \quad \overline{\mathbf{R}}\,(\mathbf{X}, t = 0) = \mathbf{1}, \quad \det\left(\overline{\mathbf{R}}\right) = 1 \tag{31}$$

The micropolar rotation field can also be expressed in terms of the axial vector field, $\overline{\phi}$, via

$$\overline{\mathbf{R}} = \exp\left(\overline{\mathbf{\Phi}}\right), \ \overline{\Phi}_{ij} = -\varepsilon_{ijk}\overline{\phi}_k \tag{32}$$

where $\overline{\mathbf{\Phi}}$ is the skew symmetric tensor associated with the axial vector $\overline{\phi}$. The three components of $\overline{\phi}$ along with the displacement field, $\mathbf{u}$, comprise the six independent degrees of freedom for the micropolar continuum. It has been shown by Eringen and Suhubi (1964) that a suitable set of invariant Lagrangian strain measures for the micropolar continuum may be defined as

$$\overline{\mathbf{U}} = \overline{\mathbf{R}}^T\mathbf{F}, \quad \mathbf{\Gamma} = \overline{\mathbf{R}}^T\left(\overline{\mathbf{R}}\nabla_0\right) \tag{33}$$

where $\overline{\mathbf{U}}$ is called the relative deformation tensor and $\mathbf{\Gamma}$ is the third-rank wryness (or torsion-curvature tensor. The Lagrangian micropolar strain is defined in terms of the relative distortion tensor as $\overline{\mathbf{E}} = \overline{\mathbf{U}} - \mathbf{1}$. Due to the antisymmetry with respect to its first two indices, it is convenient to express the torsion-curvature as a second-order tensor, i.e.,

$$\overline{K} = -\frac{1}{2}\boldsymbol{\epsilon} : \mathbf{\Gamma} \tag{34}$$

The rates of the micropolar strain and torsion-curvature tensors are related to the velocity, $\mathbf{v} = \dot{\mathbf{u}}$, and the microstructural angular velocity, $\overline{\mathbf{\Omega}} = \dot{\overline{\mathbf{R}}}\,\overline{\mathbf{R}}^T$, as

$$\dot{\overline{\mathbf{U}}}\,\overline{\mathbf{U}}^{-1} = \overline{\mathbf{R}}^T\left(\mathbf{L} - \overline{\mathbf{\Omega}}\right)\overline{\mathbf{R}} \tag{35}$$

$$\dot{\overline{K}}\,\overline{\mathbf{U}}^{-1} = \overline{\mathbf{R}}^T\left(\overline{\omega}\nabla\right)\overline{\mathbf{R}} \tag{36}$$

where $\mathbf{L} = \dot{\mathbf{F}}\mathbf{F}^{-1}$ is the velocity gradient and $\overline{\omega} = -1/2\boldsymbol{\epsilon} : \overline{\mathbf{\Omega}}$ is the axial vector associated with $\overline{\mathbf{\Omega}}$. From Eqs. (35) and (36), it is clear that the rate expressions on the LHS are pull-backs from the current configuration via the microrotation.

Thermodynamics

The mechanical balance laws under static equilibrium for the micropolar continuum are

$$\nabla \cdot \boldsymbol{\sigma}^T + \mathbf{f} = 0, \quad \nabla \cdot \mathbf{m}^T - \boldsymbol{\epsilon} : \boldsymbol{\sigma} + \mathbf{c} = 0 \tag{37}$$

where $\boldsymbol{\sigma}$ is the unsymmetric Cauchy force stress tensor, $\mathbf{f}$ is a body force vector, $\mathbf{m}$ is the couple stress tensor, and $\mathbf{c}$ is a body couple vector. These balance laws can be deduced using the principle of virtual work (Germain 1973; Forest and Sievert 2003). The energy balance and Clausius-Duhem inequality for the micropolar continuum are given, respectively, as

$$\rho \dot{U} = \boldsymbol{\sigma} : \left(\mathbf{L} - \overline{\boldsymbol{\Omega}} \right) + \mathbf{m} : \overline{\boldsymbol{\omega}} \nabla - \nabla \cdot \mathbf{q} \tag{38}$$

$$\hat{\boldsymbol{\sigma}} : \left(\dot{\overline{\mathbf{U}}} \, \overline{\mathbf{U}}^{-1} \right) + \hat{\mathbf{m}} : \left(\dot{\overline{\boldsymbol{K}}} \, \overline{\mathbf{U}}^{-1} \right) - \rho \left(\dot{\psi} + \eta \dot{T} \right) - \frac{1}{T} \mathbf{q} \cdot \nabla T \geq 0 \tag{39}$$

where $\hat{\boldsymbol{\sigma}}$ and $\hat{\mathbf{m}}$ are the Cauchy and couple stress tensors pulled back to the reference configuration via $\overline{\mathbf{R}}$, i.e.,

$$\hat{\boldsymbol{\sigma}} = \overline{\mathbf{R}}^T \boldsymbol{\sigma} \overline{\mathbf{R}}, \quad \hat{\mathbf{m}} = \overline{\mathbf{R}}^T \mathbf{m} \overline{\mathbf{R}} \tag{40}$$

The specific form of Eq. (39) was obtained by using the kinematic relations given in Eqs. (35) and (36). Let us first consider the case of finite micropolar thermoelasticity and assume that $\psi = \hat{\psi} \left(\overline{\mathbf{U}}, \overline{\boldsymbol{K}}, T \right)$. Taking the time derivative of ψ and inserting into Eq. (39) leads to

$$\left(\hat{\boldsymbol{\sigma}} \overline{\mathbf{U}}^{-T} - \rho \frac{\partial \psi}{\partial \overline{\mathbf{U}}} \right) : \dot{\overline{\mathbf{U}}} + \left(\hat{\mathbf{m}} \overline{\mathbf{U}}^{-T} - \rho \frac{\partial \psi}{\partial \overline{\boldsymbol{K}}} \right) : \dot{\overline{\boldsymbol{K}}} - \rho \left(\eta + \frac{\partial \psi}{\partial T} \right) \dot{T} \geq 0 \tag{41}$$

Therefore, the state laws for the micropolar material are

$$\hat{\boldsymbol{\sigma}} = \rho \frac{\partial \psi}{\partial \overline{\mathbf{U}}} \overline{\mathbf{U}}^T, \quad \hat{\mathbf{m}} = \rho \frac{\partial \psi}{\partial \overline{\boldsymbol{K}}} \overline{\mathbf{U}}^T, \quad \eta = -\frac{\partial \psi}{\partial T} \tag{42}$$

Next we must introduce elastic-plastic decompositions for $\overline{\mathbf{U}}$ and $\overline{\boldsymbol{K}}$. We start with the natural assumption that the hyperelastic relations will have the same form as Eq. (42) with respect to the elastic deformation measures, i.e.,

$$\hat{\boldsymbol{\sigma}} = \rho \frac{\partial \psi}{\partial \overline{\mathbf{U}}^e} \overline{\mathbf{U}}^{eT}, \quad \hat{\mathbf{m}} = \rho \frac{\partial \psi}{\partial \overline{\boldsymbol{K}}^e} \overline{\mathbf{U}}^{eT} \tag{43}$$

Consistent with this assumption, it can be shown (Sievert et al. 1998) that the appropriate decompositions are given as

$$\overline{\mathbf{U}} = \overline{\mathbf{U}}^e \overline{\mathbf{U}}^p, \quad \overline{\mathbf{K}} = \overline{\mathbf{K}}^e \overline{\mathbf{U}}^p + \overline{\mathbf{K}}^p \tag{44}$$

Substituting the rate forms of these decompositions back into the Clausius-Duhem inequality with $\psi = \hat{\psi}\left(\overline{\mathbf{U}}^e, \overline{\mathbf{K}}^e, T, \zeta^\alpha\right)$ yields

$$\Sigma : \left(\dot{\overline{\mathbf{U}}}^p \overline{\mathbf{U}}^{p-1}\right) + \mathbf{M} : \left(\dot{\overline{\mathbf{K}}}^p \overline{\mathbf{U}}^{p-1}\right) + \rho \sum_\alpha \frac{\partial \psi}{\partial \zeta^\alpha} * \dot{\zeta}^\alpha \geq 0 \tag{45}$$

where the driving forces for the plastic evolution equations are identified as

$$\Sigma = \overline{\mathbf{U}}^{eT} \hat{\boldsymbol{\sigma}} \overline{\mathbf{U}}^{e-T} + \overline{\mathbf{K}}^{eT} \hat{\mathbf{m}} \overline{\mathbf{U}}^{e-T}, \quad \mathbf{M} = \hat{\mathbf{m}} \overline{\mathbf{U}}^{e-T} \tag{46}$$

Specific constitutive equations must be provided for the free energy and plastic evolution equations to complete the formulation. The procedure for doing so can be undertaken in analogous fashion to what is done in the classical theory. However, there is some additional flexibility that is afforded in constructing the plastic evolution equations in this case compared to the classical theory (see Forest and Sievert (2003) for an in-depth discussion of single vs. multi-criterion flow rules). Rather than narrowing to specific constitutive choices in the current finite deformation context, we will discuss these issues within the small deformation framework in the subsequent sections. The principles guiding constitutive equation development are the same for both finite and infinitesimal deformations and we choose to discuss these aspects with respect to the theories used in the numerical simulations appearing later in the chapter. A more complete exposition of constitutive equation development in the finite deformation context has been given elsewhere (Forest et al. 1997; Forest 2012).

Linear Deformation Theory

Linearized Kinematics

In the case of small deformations and rotations, the following notation is introduced for the micropolar strain, $\overline{\varepsilon}$, and torsion-curvature, $\overline{\kappa}$:

$$\overline{\mathbf{E}} = \overline{\mathbf{U}} - \mathbf{1} \approx \mathbf{u}\nabla - \overline{\boldsymbol{\Phi}} =: \overline{\varepsilon} = \overline{\varepsilon}^e + \overline{\varepsilon}^p \tag{47}$$

$$\overline{\mathbf{K}} = -\frac{1}{2}\boldsymbol{\epsilon} : \boldsymbol{\Gamma} \approx \overline{\boldsymbol{\phi}}\nabla =: \overline{\kappa} = \overline{\kappa}^e + \overline{\kappa}^p \tag{48}$$

As indicated in Eqs. (47) and (48), we assume an additive elastic-plastic decomposition of the strain and torsion-curvature tensors. Note that the symmetric part of $\overline{\varepsilon}$ is the classical small strain tensor: $\mathrm{sym}\left(\overline{\epsilon}\right) = \epsilon = \mathrm{sym}\left(\mathbf{H}\right)$, and the skew-symmetric part is a measure of the difference between the continuum rotation,

$w = \text{skw}\ (\mathbf{H})$, and microrotation: $\text{skw}\ (\overline{\varepsilon}) = w - \overline{\boldsymbol{\Phi}}$. The additive decomposition of the distortion tensor, $\mathbf{H}$, into elastic and plastic parts is assumed (see section "Linearized Kinematics") and the micropolar plastic strain is defined to be equal to the plastic distortion such that the evolution equation of $\overline{\varepsilon}^{p}$ has the form

$$\dot{\overline{\varepsilon}}^{p} = \sum_{\alpha} \dot{\gamma}^{\alpha} \mathbf{s}^{\alpha} \otimes \mathbf{n}^{\alpha} \tag{49}$$

Therefore, elastic micropolar strain is defined as

$$\overline{\varepsilon}^{e} = \mathbf{H}^{e} - \overline{\boldsymbol{\Phi}} = \underbrace{\varepsilon^{e}}_{\text{sym}(\overline{\varepsilon}^{e})} + \underbrace{\left(w^{e} - \overline{\boldsymbol{\Phi}}\right)}_{\text{skw}(\overline{\varepsilon}^{e})} \tag{50}$$

Equation (50) shows that the skew-symmetric part of the micropolar elastic strain is just the difference between the lattice rotation embodied by w^{e} and the microrotation. Using the relationship between the lattice torsion-curvature and GNDs presented in section "Linearized Kinematics" as motivation, Forest et al. (1997) proposed a micropolar plastic torsion-curvature evolution equation of the form (note there is a sign convention difference between the screw GND term presented here and what was originally proposed in that work):

$$\dot{\overline{\boldsymbol{\kappa}}}^{p} = \sum_{\alpha} \left[\frac{\dot{\varphi}_{\perp}^{\alpha}}{L_{\perp}} \mathbf{t}^{\alpha} \otimes \mathbf{s}^{\alpha} + \frac{\dot{\varphi}_{\odot}^{\alpha}}{L_{\odot}} \left(\mathbf{s}^{\alpha} \otimes \mathbf{s}^{\alpha} - \frac{1}{2} \mathbf{1} \right) \right]. \tag{51}$$

Here, $\dot{\varphi}_{\perp}^{\alpha}$ and $L_{\perp}^{\alpha}$ are the plastic rotation rate and plastic length scale associated with edge GNDs and $\dot{\varphi}_{\odot}^{\alpha}$ and $L_{\odot}^{\alpha}$ are the analogous quantities for screw GNDs. Comparing Eqs. (29) and (51) reveals the relationship between the GND densities and the micropolar plastic torsion-curvature parameters, namely

$$\dot{\varrho}_{G\perp}^{\alpha} = -\frac{\dot{\varphi}_{\perp}^{\alpha}}{bL_{\perp}}, \quad \dot{\varrho}_{G\odot}^{\alpha} = -\frac{\dot{\varphi}_{\odot}^{\alpha}}{bL_{\odot}} \tag{52}$$

The introduced length scales are expected to be in the range of micron and submicron sizes as illustrated in the examples provided in this chapter.

Thermodynamics at Small Strains

Let us now revisit the Clausius-Duhem inequality for the micropolar material expressed in terms of the rates of linearized kinematic variables as a guide to constitutive equation development, i.e.,

$$\boldsymbol{\sigma} : \dot{\overline{\varepsilon}} + \mathbf{m} : \dot{\overline{\boldsymbol{\kappa}}} - \rho \left(\dot{\psi} + \eta \dot{T} \right) - \frac{1}{T} \mathbf{q} \cdot \nabla T \geq 0 \tag{53}$$

We assume a general form of the free energy that depends on the elastic strain, the elastic torsion-curvature, temperature, and a set of internal state variables, i.e.,

$\psi = \hat{\psi}\,(\overline{\varepsilon}^e, \overline{\kappa}^e, T, \zeta^\alpha)$. Taking the chain rule expression for the time derivative of $\hat{\psi}$ along with the elastic-plastic decompositions for the strain and torsion-curvature and inserting into Eq. (53) and following the Coleman-Noll procedure, the following state laws are obtained:

$$\boldsymbol{\sigma} = \rho\frac{\partial\psi}{\partial\overline{\varepsilon}^e}\ , \quad \mathbf{m} = \rho\frac{\partial\psi}{\partial\overline{\kappa}^e}\ , \quad \eta = -\frac{\partial\psi}{\partial T} \tag{54}$$

along with the expression for the intrinsic dissipation, i.e.,

$$\Delta^{intr} = \boldsymbol{\sigma} : \dot{\overline{\varepsilon}}^p + \mathbf{m} : \dot{\overline{\kappa}}^p - \sum_\alpha r^\alpha * \dot{\zeta}^\alpha \geq 0, \qquad r^\alpha = \rho\frac{\partial\psi}{\partial\zeta^\alpha} \tag{55}$$

Elastic Free Energy Function

The most general form of the elastic strain energy for a linearized micropolar continuum is given by the quadratic form viz (Eringen 1999):

$$\rho\psi_e = \frac{1}{2}\overline{\varepsilon}^e : \mathbb{C} : \overline{\varepsilon}^e + \frac{1}{2}\overline{\kappa}^e : \mathbb{D} : \overline{\kappa}^e + \overline{\varepsilon}^e : \mathbb{E} : \overline{\kappa}^e \tag{56}$$

where $\mathbb{C}$, $\mathbb{D}$, and $\mathbb{E}$ are fourth-order tensors of elastic moduli. However, the coupling moduli $\mathbb{E}$ are equal to zero for materials exhibiting point symmetry (Forest et al. 1997). Therefore, the stress and couple-stress constitutive equations for single crystals may be expressed as

$$\boldsymbol{\sigma} = \mathbb{C} : \overline{\varepsilon}^e \quad , \quad \mathbf{m} = \mathbb{D} : \overline{\kappa}^e \tag{57}$$

For an elastically isotropic material, these expressions have the form

$$\begin{aligned} \boldsymbol{\sigma} &= \lambda\ \mathrm{tr}\,(\varepsilon^e)\,\mathbf{1} + 2\mu\ \varepsilon^e + 2\mu_c\left(\boldsymbol{\omega}^e - \overline{\boldsymbol{\Phi}}\right) \\ \mathbf{m} &= \alpha\ \mathrm{tr}\,(\overline{\kappa}^e)\,\mathbf{1} + 2\beta\,\mathrm{sym}\,(\overline{\kappa}^e) + 2\gamma\,\mathrm{skw}\,(\overline{\kappa}^e) \end{aligned} \tag{58}$$

where λ and μ are the usual Lamé's constants and μ_c, α, β, and γ are nonstandard and/or higher-order elastic moduli. The coupling modulus, μ_c, gives rise to the skew symmetric part of the Cauchy stress and the couple-stress moduli, α, β, and γ, can be interpreted as elastic length scales; when they are normalized, for example, with respect to the shear modulus the resulting quantities have units of length, e.g., $\ell_e = \sqrt{\beta/\mu}$.

Flow Rules

The development of dissipative constitutive equations follows the standard approach utilizing a flow potential and associative flow rules. As discussed in Forest and Sievert (2003), one can formulate the rules either in terms of a single or multiple criteria, i.e., either a single flow potential for both strain and torsion-curvature or independent flow potentials for the respective deformation variables. Mutli-criterion

theories are more general and require the specification of additional material parameters and should only be used if there is compelling need for this additional flexibility/complexity of the model. Representative multi-criterion micropolar single crystal plasticity models were presented by Forest et al. (2000) and Mayeur and McDowell (2013). The subsequent treatment of this section will focus on a single criterion framework since the numerical results presented later in the chapter were obtained using this type of model, and we have found it to suffice for most purposes. The plastic strain and torsion-curvature evolution equations are derived from a unified slip system flow potential, $\mathcal{F}^\alpha$, i.e.,

$$\dot{\bar{\varepsilon}}^p = \sum_\alpha \dot{\lambda}^\alpha \frac{\partial \mathcal{F}^\alpha}{\partial \boldsymbol{\sigma}}, \quad \dot{\bar{\boldsymbol{\kappa}}}^p = \sum_\alpha \dot{\lambda}^\alpha \frac{\partial \mathcal{F}^\alpha}{\partial \mathbf{m}} \tag{59}$$

Given the suggested kinematic forms for the plastic strain and torsion-curvature rates (Eqs. (49) and (51)), we propose a yield function, $\mathcal{F}^\alpha$, of the form

$$\mathcal{F}^\alpha = \hat{\tau}^\alpha - (r_0 + r^\alpha) \leq 0 \tag{60}$$

Here, $\hat{\tau}^\alpha$ is an effective resolved shear stress and r_0 is the initial yield strength. The effective resolved shear stress is defined with respect to the projections of the force and couple stress tensors as

$$\hat{\tau}^\alpha = \sqrt{\left| \tau_{eff}^\alpha \right|^2 + \left| \pi_\perp^\alpha / L_\perp \right|^2 + \left| \pi_\odot^\alpha / L_\odot \right|^2}. \tag{61}$$

where τ_{eff}^α is the resolved shear stress, $\pi_\perp$ is the resolved couple stress acting on edge GNDs, $\pi_\odot$ is the resolved couple stress acting on screw GNDs, and $L_\perp$, $L_\odot$ are normalizing length scales for edge and screw GNDs, respectively. The resolved shear and couple stresses are defined as

$$\tau_{eff}^\alpha = \boldsymbol{\sigma} : (\mathbf{s}^\alpha \otimes \mathbf{n}^\alpha) \tag{62}$$

$$\pi_\perp^\alpha = \mathbf{m} : (\mathbf{t}^\alpha \otimes \mathbf{s}^\alpha) \tag{63}$$

$$\pi_\odot^\alpha = \mathbf{m} : \left(\mathbf{s}^\alpha \otimes \mathbf{s}^\alpha - \frac{1}{2}\mathbf{1} \right) \tag{64}$$

The "*eff*" subscript has been applied to the resolved shear stress to emphasize that the driving force for slip has a contribution from the skew-symmetric part of the stress tensor and also to distinguish it from the classical resolved shear stress, which is computed using only the symmetric part of the Cauchy stress. The contribution of the skew-symmetric part of the Cauchy stress to τ_{eff}^α gives rise to gradient-dependent kinematic hardening which is elaborated upon further in section "Relationship to Slip Gradient Theory." The flow directions then follow as

$$\frac{\partial \mathcal{F}^\alpha}{\partial \boldsymbol{\sigma}} = \frac{\tau_{eff}^\alpha}{\hat{\tau}^\alpha} \mathbf{s}^\alpha \otimes \mathbf{n}^\alpha \tag{65}$$

$$\frac{\partial \mathcal{F}^\alpha}{\partial \mathbf{m}} = \frac{1}{L_\perp} \mathbf{t}^\alpha \otimes \mathbf{s}^\alpha \frac{\pi_\perp^\alpha / L_\perp}{\hat{\tau}^\alpha} + \frac{1}{L_\odot} \left(\mathbf{s}^\alpha \otimes \mathbf{s}^\alpha - \frac{1}{2} \mathbf{1} \right) \frac{\pi_\odot^\alpha / L_\odot}{\hat{\tau}^\alpha}. \tag{66}$$

Herein, we work within an elastic-viscoplastic setting and propose a power law expression for $\dot{\lambda}^\alpha$, i.e.,

$$\dot{\lambda}^\alpha = \dot{\lambda}_0 \left\langle \frac{\hat{\tau}^\alpha - (r_0 + r^\alpha)}{g^\alpha} \right\rangle^m \tag{67}$$

where $\dot{\lambda}_0$ is a reference effective deformation rate, g^α is a viscous drag stress, and m is an inverse rate sensitivity exponent. Inserting Eqs. (65), (66), and (67) into Eq. (59) and comparing with the expressions given in Eqs. (49) and (51), the expressions for the slip system deformation rates are obtained as

$$\dot{\gamma}^\alpha = \dot{\lambda}_0 \left\langle \frac{\hat{\tau}^\alpha - (r_0 + r^\alpha)}{g^\alpha} \right\rangle^m \frac{\tau_{eff}^\alpha}{\hat{\tau}^\alpha} \tag{68}$$

$$\dot{\varphi}_\perp^\alpha = \dot{\lambda}_0 \left\langle \frac{\hat{\tau}^\alpha - (r_0 + r^\alpha)}{g^\alpha} \right\rangle^m \frac{\pi_\perp^\alpha / L_\perp}{\hat{\tau}^\alpha} \tag{69}$$

$$\dot{\varphi}_\odot^\alpha = \dot{\lambda}_0 \left\langle \frac{\hat{\tau}^\alpha - (r_0 + r^\alpha)}{g^\alpha} \right\rangle^m \frac{\pi_\odot^\alpha / L_\odot}{\hat{\tau}^\alpha} \tag{70}$$

It is easily shown from Eqs. (68), (69), and (70) that the slip system plastic multiplier is related to the slip and curvature rates as

$$\dot{\lambda}^\alpha = \sqrt{|\dot{\gamma}^\alpha|^2 + |\dot{\varphi}_\perp^\alpha|^2 + |\dot{\varphi}_\odot^\alpha|^2} \tag{71}$$

Equation (71) reveals that $\dot{\lambda}^\alpha$ is an effective slip system deformation rate accounting for both slip and torsion-curvature deformation modes.

Internal State Variable Evolution

Consider the case where the evolution of the internal state variable associated with energetic isotropic hardening with the effective deformation rate, i.e.,

$$\dot{\varsigma}^\alpha = \dot{\lambda}^\alpha \tag{72}$$

Further, a quadratic dependence of the free energy on ς^α is assumed

$$\rho \psi_{in} = \frac{1}{2} \sum_\alpha \sum_\beta \mathrm{H}^{\alpha\beta} \varsigma^\alpha \varsigma^\beta, \quad \mathrm{H}^{\alpha\beta} = H_0 \tag{73}$$

where $H^{\alpha\beta}$ is the hardening matrix and $H_0 > 0$ is the hardening modulus. The energetic isotropic hardening stress is then given as

$$r^\alpha = \sum_\beta H^{\alpha\beta} \varsigma^\beta = H_0 \sum_\beta \varsigma^\beta \tag{74}$$

Given the preceding evolution equations, the intrinsic dissipation inequality may now be expressed in terms of slip system variables as

$$\Delta^{intr} = \sum_\alpha \left(\tau_{eff}^\alpha \dot{\gamma}^\alpha + \pi_\perp^\alpha \frac{\dot{\varphi}_\perp^\alpha}{L_\perp} + \pi_\odot^\alpha \frac{\dot{\varphi}_\odot^\alpha}{L_\odot} - r^\alpha \varsigma^\alpha \right) \geq 0 \tag{75}$$

which may be further simplified and expressed as

$$\Delta = \sum_\alpha (\hat{\tau}^\alpha - r^\alpha) \dot{\lambda}^\alpha \geq 0 \tag{76}$$

For nonzero values of $\dot{\lambda}^\alpha$, Eq. (67) can be inverted to obtain the expression for $\hat{\tau}^\alpha$ as

$$\hat{\tau}^\alpha = g^\alpha \left(\frac{\dot{\lambda}^\alpha}{\dot{\lambda}_0} \right)^{\frac{1}{m}} + r_0 + r^\alpha \tag{77}$$

Inserting this expression into Eq. (76) yields

$$\Delta^{intr} = \sum_\alpha \left[g^\alpha \left(\frac{\dot{\lambda}^\alpha}{\dot{\lambda}_0} \right)^{\frac{1}{m}} + r_0 \right] \dot{\lambda}^\alpha \geq 0 \tag{78}$$

Therefore, the dissipation inequality is unconditionally satisfied for this set of constitutive equations.

While the illustrative example given in this particular section yields a simple linear isotropic hardening behavior, it is straightforward and often preferable in practice to use nonlinear hardening laws; general examples of such extensions were previously given by Forest et al. (1997) and Mayeur et al. (2011). In the sequel, we present a dislocation density-based hardening framework (Mayeur and McDowell 2013) that has been compared to a number discrete dislocation dynamics boundary value problems; some of which will be presented as representative applications of the theory.

Dislocation Density-Based Strength Model

Previously, Mayeur et al. (2011) and Mayeur and McDowell (2013) have employed both single and mutli-criterion flow rules with a variety of hardening laws to simulate size-dependent behavior observed in 2D discrete dislocation dynamics

(DDD) simulations to varying degrees of success. The hardening model presented is the simplest version capable of reproducing the observed DDD behavior.

We take the statistically stored dislocation density on each slip system, ϱ_S^α, as our primary internal state variable to describe the hardening behavior. The slip system yield stress is defined in terms of a Taylor relation that is assumed to depend only on the SSD density, i.e.,

$$r^\alpha = r_0 + c_1 \mu b \sqrt{\sum_\beta h^{\alpha\beta} \varrho_S^\beta} \tag{79}$$

where c_1 is a constant, b is the Burgers vector, and $h^{\alpha\beta}$ is an interaction matrix. We do not use a generalized Taylor relation that directly includes a dependence on the GND density, which is a commonly employed assumption in other classes of generalized single crystal models. It was shown (Mayeur and McDowell 2013) that a hardening model based on the generalized Taylor relation leads to excessive and unrealistic hardening as compared to the DDD simulations. The SSD density evolves according to a Kocks-Mecking (Mecking and Kocks 1981) relation which represents a competition between storage and recovery mechanisms until the steady-state value of dislocation density is reached:

$$\dot{\varrho}_S^\alpha = \frac{1}{b} \left(\frac{1}{\Lambda^\alpha} - 2 y_c \varrho_S^\alpha \right) \dot{\lambda}^\alpha \tag{80}$$

Here, Λ^α is the mean free path between dislocations, and y_c is the capture radius for dislocation annihilation. The mean free path is defined in terms of the SSD density, an average dislocation junction strength, K, and an interaction matrix, $a^{\alpha\beta}$ as

$$\Lambda^\alpha = \frac{K}{\sqrt{\sum_\beta a^{\alpha\beta} \varrho_S^\beta}} \tag{81}$$

Since the SSD evolution equation is defined with respect to $\dot{\lambda}^\alpha$ rather than $\dot{\gamma}^\alpha$, it naturally includes scale-dependence by virtue of $\dot{\lambda}^\alpha$ being an effective slip system deformation measure (see Eq. (71)). We found this type of scale-dependent isotropic hardening described the DDD results better than either a direct dependence of the Taylor stress and/or the mean free path on the GND density. We note that size effects of initial yield stress, r_0, are not addressed by the hardening relations and may depend on the initial dislocation source distribution as well as obstacles and interfaces that impede slip.

Relationship to Slip Gradient Theory

In this section, we briefly discuss the relationship of micropolar crystal plasticity to slip gradient crystal plasticity theory in the form developed by Gurtin (2002, 2007).

A more in-depth comparison of the two model frameworks and simulation results has been given by Mayeur and McDowell (2014). Gurtin's theory is based on taking the slip system shears as continuum degrees of freedom and contains an additional balance equation – the so-called microforce balance – in addition to the classical force and angular momentum balances. The microforce balance is given as

$$\tau^\alpha + \nabla \cdot \boldsymbol{\xi}^\alpha - q^\alpha = 0 \tag{82}$$

where τ^α is the classical resolved shear stress, $\boldsymbol{\xi}^\alpha$ is a higher-order stress that is power-conjugate to the slip rate gradient, $\nabla \dot{\gamma}^\alpha$, and q^α is the stress power-conjugate to the slip rate, $\dot{\gamma}^\alpha$. In addition to Dirichlet micro-boundary conditions on the slip system shears, complementary micro-traction boundary conditions may also be prescribed in terms of the micro-traction Ξ^α, i.e.,

$$\Xi^\alpha = \boldsymbol{\xi}^\alpha \cdot \mathbf{n} \tag{83}$$

The macroscopic and microscopic scales are coupled by the presence of the resolved shear stress, $\tau^\alpha = \mathbf{n}^\alpha \cdot \boldsymbol{\sigma} \cdot \mathbf{s}^\alpha$, in the microforce balance. The microforce balance is a partial differential equation that governs the evolution of the slip system shears and can be interpreted as a nonlocal yield condition.

Thermodynamics

Thermodynamically consistent constitutive equations have been developed by Gurtin using a purely mechanical form of the 2nd law, i.e.,

$$\Delta^{intr} = \boldsymbol{\sigma} : \dot{\varepsilon}^e + \sum_\alpha (q^\alpha \dot{\gamma}^\alpha + \boldsymbol{\xi}^\alpha \cdot \nabla \dot{\gamma}^\alpha) - \dot{\psi} \geq 0 \tag{84}$$

The free energy is assumed to depend on the elastic strain and the set of slip system shear gradients, $\nabla \vec{\gamma} = \{\nabla \gamma^1, \ldots, \nabla \gamma^N\}$, i.e.,

$$\psi = \hat{\psi}\left(\varepsilon^e, \nabla \vec{\gamma}\right) = \hat{\psi}_e\left(\varepsilon^e\right) + \hat{\psi}_{in}\left(\nabla \vec{\gamma}\right) \tag{85}$$

Expressing the time derivative of the free energy via the chain rule and inserting into Eq. (84) yields

$$\Delta^{intr} = \left(\boldsymbol{\sigma} - \frac{\partial \psi}{\partial \varepsilon^e}\right) : \dot{\varepsilon}^e + \sum_\alpha \left[q^\alpha \dot{\gamma}^\alpha + \left(\boldsymbol{\xi}^\alpha - \frac{\partial \psi}{\partial \nabla \gamma^\alpha}\right) \cdot \nabla \dot{\gamma}^\alpha\right] \geq 0 \tag{86}$$

It is assumed that $\boldsymbol{\xi}^\alpha$ can be decomposed additively into energetic and dissipative components such that

$$\boldsymbol{\xi}^\alpha = \boldsymbol{\xi}^\alpha_{en} + \boldsymbol{\xi}^\alpha_d, \quad \boldsymbol{\xi}^\alpha_{en} \doteq \frac{\partial \psi}{\partial \nabla \gamma^\alpha} \tag{87}$$

Following the Coleman-Gurtin (Coleman and Gurtin 1967) thermodynamic procedure, the state law for the Cauchy stress obtained is identical to that of Eq. $(54)_1$. Making use of Eq. (87), the reduced dissipation inequality is given as

$$\Delta^{intr} = \sum_{\alpha} \left(q^{\alpha} \dot{\gamma}^{\alpha} + \boldsymbol{\xi}_d^{\alpha} \cdot \nabla \dot{\gamma}^{\alpha} \right) \geq 0 \qquad (88)$$

Classical quadratic elastic free energy potentials are employed within the Gurtin-type theory since the treatment of the macroscopic forces is unaltered. Representative constitutive equations for the defect energy and dissipative stresses are presented below.

Energetic Constitutive Equations (Defect Energy)

Several variations of the defect energy have been proposed in the literature and can be classified as either recoverable or nonrecoverable. A recoverable defect energy depends on the current values of the slip gradients and vanishes when there are no slip gradients regardless of prior loading history, whereas a nonrecoverable energy does not vanish upon unloading. A typical recoverable defect energy is given as (Reddy 2011)

$$\psi_d = \frac{1}{2} g_0 \ell_{en}^2 \sum_{\alpha} \left[c_{\vdash} \left(\tilde{\varrho}_{\vdash}^{\alpha} \right)^2 + c_{\odot} \left(\tilde{\varrho}_{\odot}^{\alpha} \right)^2 \right] \qquad (89)$$

where g_0 is the initial flow stress, ℓ_{en} is an energetic length scale, and $c_{\vdash}/c_{\odot}$ are dimensionless constants defining the relative contributions of edge and screw GNDs, respectively. The edge and screw GND measures used in Eq. (89) are defined as

$$\tilde{\varrho}_{\vdash}^{\alpha} = -\nabla \gamma^{\alpha} \cdot \mathbf{s}^{\alpha}, \qquad \tilde{\varrho}_{\odot}^{\alpha} = -\nabla \gamma^{\alpha} \cdot \mathbf{t}^{\alpha} \qquad (90)$$

Note the dimensional and sign difference of the screw GND term with respect to the GND density definitions used in section "Linearized Kinematics." The energetic microcouple stress vector corresponding to ψ_d is given as

$$\boldsymbol{\xi}_{en}^{\alpha} = -g_0 \ell_{en}^2 \left(c_{\vdash} \tilde{\varrho}_{\vdash}^{\alpha} \mathbf{s}^{\alpha} + c_{\odot} \tilde{\varrho}_{\odot}^{\alpha} \mathbf{t}^{\alpha} \right) \qquad (91)$$

The microcouple stress vector lies in the slip plane and decomposes naturally into edge and screw components. Gurtin et al. (2007) view $\boldsymbol{\xi}_{en}^{\alpha}$ as reflective of a net distributed Peach-Koehler force acting on the GNDs since its components are perpendicular to the respective dislocation line directions and have units of force per unit length.

Dissipative Constitutive Equations

The dissipative constitutive equations are introduced with the aid of an effective slip system deformation rate, d^{α}, defined as

$$d^{\alpha} = \sqrt{|\dot{\gamma}^{\alpha}|^2 + L_d^2 \|\nabla_{\tan}^{\alpha} \dot{\gamma}^{\alpha}\|^2} \qquad (92)$$

where L_d is a dissipative length scale and the tangential gradient operator is defined as $\nabla^\alpha_{\tan} f = (\nabla f \cdot \mathbf{s}^\alpha) \, \mathbf{s}^\alpha + (\nabla f \cdot \mathbf{t}^\alpha) \, \mathbf{t}^\alpha$. The scalar dissipative microstress is posited to have the functional form

$$q^\alpha = g^\alpha \left(\frac{d^\alpha}{d_0} \right)^{\frac{1}{m}} \frac{\dot{\gamma}^\alpha}{d^\alpha} \tag{93}$$

where g^α is a viscous drag stress, d_0 is the reference effective deformation rate, and m is the inverse rate-sensitivity exponent. The dissipative microcouple stress is introduced in an analogous manner, i.e.,

$$\boldsymbol{\xi}^\alpha_d = g^\alpha L_d^2 \left(\frac{d^\alpha}{d_0} \right)^{\frac{1}{m}} \frac{\nabla^\alpha_{\tan} \dot{\gamma}^\alpha}{d^\alpha} \tag{94}$$

Inserting Eqs. (93) and (94) into Eq. (88) and making use of Eq. (92) yields

$$\Delta^{intr} = \sum_\alpha \tilde{\tau}^\alpha d^\alpha \geq 0, \quad \tilde{\tau}^\alpha := g^\alpha \left(\frac{d^\alpha}{d_0} \right)^{\frac{1}{m}}. \tag{95}$$

Here, we introduce the implicitly defined effective dissipative stress, $\tilde{\tau}^\alpha$, that is power-conjugate to the effective slip system deformation rate d^α. It is straightforward to show that $\tilde{\tau}^\alpha$ can also be expressed in terms of the dissipative microstresses, i.e.,

$$\tilde{\tau}^\alpha = \left[(q^\alpha)^2 + \| \boldsymbol{\xi}^\alpha_d / L_d \|^2 \right]^{1/2}. \tag{96}$$

Inverted Flow Rule Versus Microforce Balance

An examination of the micropolar and slip gradient theories reveals many similarities between the two sets of governing equations. Central to both theories is the notion that the presence of GNDs gives rise to both energetic and dissipative contributions to scale-dependent mechanical behavior. In general, nonlocal strengthening effects are manifested in both the isotropic and kinematic hardening responses of the material. A key component of the slip gradient theory is the microforce balance, which couples the macroscopic and microscopic responses and represents a nonlocal flow rule governing the evolution of the slip system shears. Typically, the $\nabla \cdot \boldsymbol{\xi}^\alpha$ term in the microforce balance induces kinematic hardening and the q^α term leads to isotropic hardening, although the exact nature of the hardening contributions depends on the specific constitutive forms employed. The noteworthy feature of second term in the microforce balance is that it is a function of second gradients of slip since $\boldsymbol{\xi}^\alpha = f\left(\nabla^\alpha_{\tan} \gamma^\alpha \right)$. The relationship between second gradients of slip (GND gradients) and kinematic hardening is in accordance with other dislocation-based gradient single crystal plasticity theories (Yefimov et al. 2004a; Evers et al. 2004; Forest 2008).

A similar result is obtained for the micropolar theory by considering the inverted flow rule, which is obtained from the coaxiality relations $\tau_{eff}^\alpha / \hat{\tau}^\alpha = \dot{\gamma}^\alpha / \dot{\lambda}^\alpha$. Neglecting the isotropic energetic hardening terms in Eq. (77), the coaxiality relations may be rearranged and expressed as

$$\tau^\alpha + \tau_b^\alpha - g^\alpha \left(\frac{\dot{\lambda}^\alpha}{\dot{\lambda}_0} \right)^{\frac{1}{m}} \frac{\dot{\gamma}^\alpha}{\dot{\lambda}^\alpha} = 0. \tag{97}$$

Here, the resolved Cauchy stress, τ_{eff}^α, is explicitly written as two terms where the second term is a back stress, $\tau_b^\alpha := \frac{1}{2} \mathbf{t}^\alpha \cdot \left(\nabla \cdot \mathbf{m}^\mathrm{T} \right)$, related to the projection of the skew symmetric part of the stress tensor. The back stress may be expressed as a function of the couple stress since $2 \ \mathrm{skw}(\boldsymbol{\sigma}) = \boldsymbol{\epsilon} \cdot (\nabla \cdot \mathbf{m}^\mathrm{T})$. Thus, the back stress in the micropolar theory is a function of lattice torsion-curvature gradients. This is analogous to the dependence exhibited by the slip gradient theory since second gradients of slip (GND gradients) are directly connected to lattice torsion-curvature gradients via Nye's relations (see section "Linearized Kinematics"). In both theories, the higher-order balance law leads to the coupling of the micro and macro scales and to the natural inclusion of gradient-dependent kinematic hardening. Compare Eq. (97) to the microforce balance augmented with the constitutive equation for q^α given in Eq. (93)

$$\tau^\alpha + \nabla \cdot \boldsymbol{\xi}^\alpha - \tilde{g}^\alpha \left(\frac{d^\alpha}{d_0} \right)^{\frac{1}{m}} \frac{\dot{\gamma}^\alpha}{d^\alpha} = 0. \tag{98}$$

The similarities between the two expressions given in Eqs. (97) and (98) are obvious, although some key differences emerge when the constitutive equations for $\mathbf{m}$ and $\boldsymbol{\xi}^\alpha$ are considered. To illustrate these differences, we compare the microforce balance and inverted micropolar flow rule augmented with simple constitutive equations for the 2D case (e.g., edge dislocations only). Inserting Eqs. (91) and (94) into Eq. (98), the following expression is obtained:

$$\tau^\alpha + g_0 \ell_{en}^2 c_\vdash \nabla \cdot \left[(\nabla \gamma^\alpha \cdot \mathbf{s}^\alpha) \, \mathbf{s}^\alpha \right] + L_d^2 \nabla \cdot \left[g^\alpha \left(\frac{d^\alpha}{d_0} \right)^{\frac{1}{m}} \frac{(\nabla \dot{\gamma}^\alpha \cdot \mathbf{s}^\alpha) \, \mathbf{s}^\alpha}{d^\alpha} \right]$$
$$- g^\alpha \left(\frac{d^\alpha}{d_0} \right)^{\frac{1}{m}} \frac{\dot{\gamma}^\alpha}{d^\alpha} = 0. \tag{99}$$

An analogous expression for the inverted micropolar flow rule is obtained by using a simplified version of Eq. (58)$_2$ where $\mathbf{m} = 2\mu \ell_e^2 \overline{\boldsymbol{\kappa}}^e$ in Eq. (97), i.e.,

$$\tau^\alpha + \mu \ell_e^2 \mathbf{t}^\alpha \cdot \left(\nabla \cdot \overline{\boldsymbol{\kappa}}^\mathrm{T} \right) - \frac{\mu \ell_e^2}{L_\perp} \mathbf{t}^\alpha \cdot \left(\nabla \cdot \sum_\beta \varphi_\perp^\beta \mathbf{s}^\beta \otimes \mathbf{t}^\beta \right) - g^\alpha \left(\frac{\dot{\lambda}^\alpha}{\dot{\lambda}_0} \right)^{\frac{1}{m}} \frac{\dot{\gamma}^\alpha}{\dot{\lambda}^\alpha} = 0. \tag{100}$$

Note that the energetic and dissipative length scales appear isolated in separate terms in Eq. (99), whereas the third term in Eq. (100) contains both the elastic and plastic length scales. Therefore, both energetic and dissipative gradient effects are eliminated when $\ell_e = 0$ in the micropolar theory; however, the dissipative gradient term is suppressed for $L_\perp \gg \ell_e^2$ irrespective of the value of ℓ_e. The separation of energetic and dissipative gradient hardening terms in the slip gradient theory is a direct consequence of the assumed additive decomposition of $\boldsymbol{\xi}$. Another, perhaps more subtle, difference between the two expressions is that the dissipative gradient term in the microforce balance is a function of slip rate gradients, while it is a function of total plastic curvature in the inverted micropolar flow rule. We remark that if the micropolar theory was cast in terms of an additive energetic/dissipative decomposition of the couple stress tensor rather than an additive elastic-plastic decomposition of the torsion-curvature tensor, the micropolar model would mirror the phenomenology of the slip gradient model in terms of a strict separation of energetic and dissipative gradient hardening effects, and the dissipative gradient hardening would be proportional to the rate of lattice torsion curvature.

Curvatures, Couple Stresses, and Gradient Terms

With the connection between the vectorial microcouple stress, $\boldsymbol{\xi}^\alpha$, and the second rank couple stress tensor, $\mathbf{m}$, established, additional analogies between the two models are explored. A comparison of Eqs. (90) and (52) reveals a relationship between the micropolar plastic torsion-curvature flow rates and the directional slip gradients, i.e.,

$$\dot{\varphi}_\perp^\alpha \leftrightarrow L_d \nabla \dot{\gamma}^\alpha \cdot \mathbf{s}^\alpha \quad , \quad \dot{\varphi}_\odot^\alpha \leftrightarrow L_d \nabla \dot{\gamma}^\alpha \cdot \mathbf{t}^\alpha \tag{101}$$

where $\leftrightarrow$ is used to signify that the two terms have analogous roles in the respective theories. This association is further evident when the effective deformation rate in Eq. (92) is expressed in component form as

$$d^\alpha = \sqrt{|\dot{\gamma}^\alpha|^2 + |L_d \nabla \dot{\gamma}^\alpha \cdot \mathbf{s}^\alpha|^2 + |L_d \nabla \dot{\gamma}^\alpha \cdot \mathbf{t}^\alpha|^2}. \tag{102}$$

which establishes $d^\alpha \leftrightarrow \dot{\lambda}^\alpha$ (see Eq. (71)). If the energetic isotropic hardening term in Eq. (76) is neglected and compared to the analogous expression in Eq. (95), we see that the two dissipation inequalities have identical forms. Therefore, it is straightforward to show that the resolved couple stresses in the micropolar theory can be related to the dissipative microcouple stresses of the slip gradient theory by expressing the dissipation inequality in a form that parallels Eq. (75). First, the dissipative constitutive equation for $\boldsymbol{\xi}_d^\alpha$ given in Eq. (94) is written in component form as

$$\boldsymbol{\xi}_d^\alpha = g^\alpha L_d^2 \left(\frac{d^\alpha}{d_0} \right)^{\frac{1}{m}} \frac{(\nabla \dot{\gamma}^\alpha \cdot \mathbf{s}^\alpha) \, \mathbf{s}^\alpha + (\nabla \dot{\gamma}^\alpha \cdot \mathbf{t}^\alpha) \, \mathbf{t}^\alpha}{d^\alpha} = \xi_{d\vdash}^\alpha \mathbf{s}^\alpha + \xi_{d\odot}^\alpha \mathbf{t}^\alpha \tag{103}$$

where $\xi_{d\vdash}^{\alpha}$ and $\xi_{d\odot}^{\alpha}$ are the edge and screw components of $\boldsymbol{\xi}_d^{\alpha}$. Inserting Eq. (103) into Eq. (88) and making use of the microforce balance, the dissipation inequality may be expressed as

$$\Delta^{intr} = \sum_{\alpha} \left[(\tau^{\alpha} + \nabla \cdot \boldsymbol{\xi}^{\alpha}) \dot{\gamma}^{\alpha} + \frac{\xi_{d\vdash}^{\alpha}}{L_d} (L_d \nabla \dot{\gamma}^{\alpha} \cdot \mathbf{s}^{\alpha}) + \frac{\xi_{d\odot}^{\alpha}}{L_d} (L_d \nabla \dot{\gamma}^{\alpha} \cdot \mathbf{t}^{\alpha}) \right] \geq 0. \tag{104}$$

A comparison of Eqs. (75) and (104) in conjunction with the relationships identified in Eq. (101) reveals that

$$\tau_{eff}^{\alpha} \leftrightarrow \tau^{\alpha} + \nabla \cdot \boldsymbol{\xi}^{\alpha} \tag{105}$$

$$\pi_{\perp}^{\alpha}/L_{\perp} \leftrightarrow \xi_{d\vdash}^{\alpha}/L_d \tag{106}$$

$$\pi_{\odot}^{\alpha}/L_{\odot} \leftrightarrow \xi_{d\odot}^{\alpha}/L_d \tag{107}$$

The association established in Eq. (105) was already apparent from a comparison of the inverted micropolar flow rule and the microforce balance, whereas the relationships established by Eqs. (106) and (107) were revealed by inserting the component form of $\boldsymbol{\xi}_d^{\alpha}$ into the reduced dissipation inequality. Furthermore, we can rewrite the effective dissipative stress in the slip gradient theory using the component form of $\boldsymbol{\xi}_d^{\alpha}$ as

$$\tilde{\tau}^{\alpha} = \sqrt{|\tau^{\alpha} + \nabla \cdot \boldsymbol{\xi}^{\alpha}|^2 + \left|\xi_{d\vdash}^{\alpha}/L_d\right|^2 + \left|\xi_{d\odot}^{\alpha}/L_d\right|^2}. \tag{108}$$

This expression is consistent with Eq. (61) of the micropolar theory given the relationships established by Eqs. (105), (106), and (107).

As a final remark, we remind the reader that the micropolar theory differs from slip gradient theory by its adoption of the rotation of the microstructure director vectors in Eq. (30) as an independent constitutive prescription. This also simplifies the numerical implementation since slip gradients need not be computed or estimated. The remainder of section "Micropolar Single Crystal Plasticity" explores applications of this single crystal micropolar framework. The chapter dedicated to micromorphic crystal plasticity considers further extension of the micropolar theory to a micromorphic theory that includes distortion of the director vectors.

Applications: Comparison to 2D Discrete Dislocation Dynamics Simulations

This section presents a comparison of two-dimensional micropolar crystal plasticity and discrete dislocation dynamics simulations of single crystal thin films subjected to a variety of loading conditions. Specifically, we examine three widely studied

boundary value problems: constrained simple shear, pure bending (single and double slip configurations), and simple shear of a particle reinforced composite. These problems are routinely used as benchmarks to evaluate the ability of generalized single crystal plasticity models to accurately capture size effects. A micropolar single crystal model with the hardening described by Eqs. (79), (80), and (81) was implemented in an Abaqus/Standard Version 6.7.1 (2007) user element subroutine (UEL) for the simulations presented below. The element is a four node quadrilateral and the integration is performed using a B-bar technique to prevent volumetric locking. Both the displacement and rotation fields are interpolated using standard bilinear shape functions.

The micropolar model has been independently calibrated for each boundary value problem by fitting to both average (e.g., stress-strain curves) and microscopic (e.g., dislocation density distributions) deformation behavior. It was previously demonstrated that fitting to multiple aspects of the deformation behavior is necessary to obtain a unique set of micropolar constitutive parameters (Mayeur et al. 2011). As a result of the 2D nature of the problems considered, the calibration procedure is simplified in the sense that there are only a few parameters to be determined. Essentially, there are four fitting parameters that are summarized by the set: $M = \{r_0, K, \ell_e, L_\perp\}$. All of the other material parameters are either known as inputs (e.g., classical elastic parameters, Burgers vector magnitude) or can be assigned standard values based on experience from classical local crystal plasticity models. For example, the viscoplastic parameters $\left(\dot{\lambda}^\alpha, g^\alpha, m\right)$ cannot be explicitly determined due to lack of DDD results at multiple strain rates, so reasonable values for these parameters are prescribed and held fixed throughout the calibration process. Note that only a single elastic and plastic length must be determined. For plane strain problems, the couple stress constitutive relation given in Eq. (58)$_2$ reduces to

$$m_{3i} = 2\beta\overline{\kappa}^e_{3i} = 2\mu\ell_e^2\overline{\kappa}^e_{3i}, \quad i = 1, 2, \tag{109}$$

where it has been assumed, without loss of generality, that $\beta = \gamma$. Recall, the couple stress constitutive parameter, β, is related to an elastic length scale parameter, $\ell_e = \sqrt{\beta/\mu}$. As discussed by Forest (2008), the nonclassical elastic constant, μ_c, Eq. (58)$_1$, is not a free fitting parameter in micropolar single crystal plasticity. Rather, it serves as an internal penalty constraint forcing the lattice rotations to coincide with the rotational part of the elastic distortion. Because of this constraint, the micropolar torsion-curvature is identified as the lattice torsion-curvature thereby making the connection between GNDs and the scale effects predicted by the model. Since screw GNDs do not contribute to plastic torsion-curvature evolution in the 2D boundary value problems, there is a single plastic length scale parameter, $L_\perp$, to be determined.

Here, we briefly outline how the length scale parameters affect material response a general strategy for calibrating them to the DDD simulations. The elastic length scale parameter, ℓ_e, is related to the initial scale-dependent kinematic hardening

modulus and the ratio $L_\perp/\ell_e$ dictates the saturation rate of gradient hardening. Larger $L_\perp/\ell_e$ ratios are associated with slower transients such that when $L_\perp \gg \ell_e$, the strengthening effect reduces to that of linear gradient kinematic hardening (Mayeur et al. 2011). The elastic length scale should also be small enough so as not to induce size-dependent effects in the elastic deformation regime. The plastic length scale, $L_\perp$, determines the magnitude of the GND density distributions; however, its influence is not independent of the prescribed value of ℓ_e. As shown in Mayeur et al. (2011), it is the ratio $L_\perp/\ell_e$ that dictates the maximum value of the local GND density fields. If ℓ_e is varied while holding $L_\perp/\ell_e$ and all other model parameters constant (including specimen dimensions), the resulting GND density field will be essentially unchanged. To illustrate how the length scale parameters influence the average stress strain response, we show two plots in Fig. 1 where the elastic length scale is varied while keeping the ratio $L_\perp/\ell_e$ fixed (here $L_p = L_\perp$) and another with fixed elastic length scale and varying $L_\perp/\ell_e$ for the problem of constrained simple shear (Mayeur and McDowell 2014).

The parameter r_0 is used to fit to the initial yield strength rather than a prescribed initial dislocation density since the DDD simulations are assumed to be initially dislocation free. However, in the planar double slip simulations, a negligibly small value of initial SSD density (10^{-6} μm^{-2}) is specified for each slip system so that SSD evolution is nonzero. This approach is taken in lieu of introducing a nucleation term in the SSD density evolution equation. It is worth mentioning that r_0 should not necessarily be treated as a fixed material constant due to the statistical variations in the source strength and spatial distribution in the discrete dislocation simulations, as well as the mean free path of initial obstacles or impenetrable interfaces. The initial yield point in the discrete simulations will depend significantly on the availability of weak sources in highly stressed regions. Given a fixed value for the initial slip system yield strength, approximate upper bounds can be established for ℓ_e and K by isolating the effects of the two distinct material strengthening mechanisms. For example, given a target stress-strain curve, the maximum value of ℓ_e is determined by assuming that all of the material hardening is due to the gradient-induced back stresses ($1/K = 0$), whereas the maximum value of K is determined by assuming that all of the material hardening is due to slip threshold hardening ($\ell_e = 0$). In general, both mechanisms will contribute to the material strengthening and the actual values will fall below the upper bounds. As discussed in Mayeur and McDowell (2013), either the unloading behavior or some other attribute of the local deformation field (e.g., shear strain distributions) must be used in order to differentiate between the relative hardening contributions. A list of micropolar constitutive parameters used in all of the simulations is given in Table 1.

Constrained Shear of Thin Films

Here, we compare results of the micropolar model to DDD results for a constrained thin film subjected to simple shear originally presented by Shu et al. (2001). Related studies were also conducted by Yefimov and van der Giessen (2005b)

Fig. 1 Average shear
stress-strain response for
constrained simple shear with
(**a**) different values of L_p/ℓ_e
with $\ell_e = 100$ nm and (**b**)
different elastic length scale
parameters with $L_p/\ell_e = 5$.
Slip threshold hardening is
suppressed ($r^\alpha = r_0$)
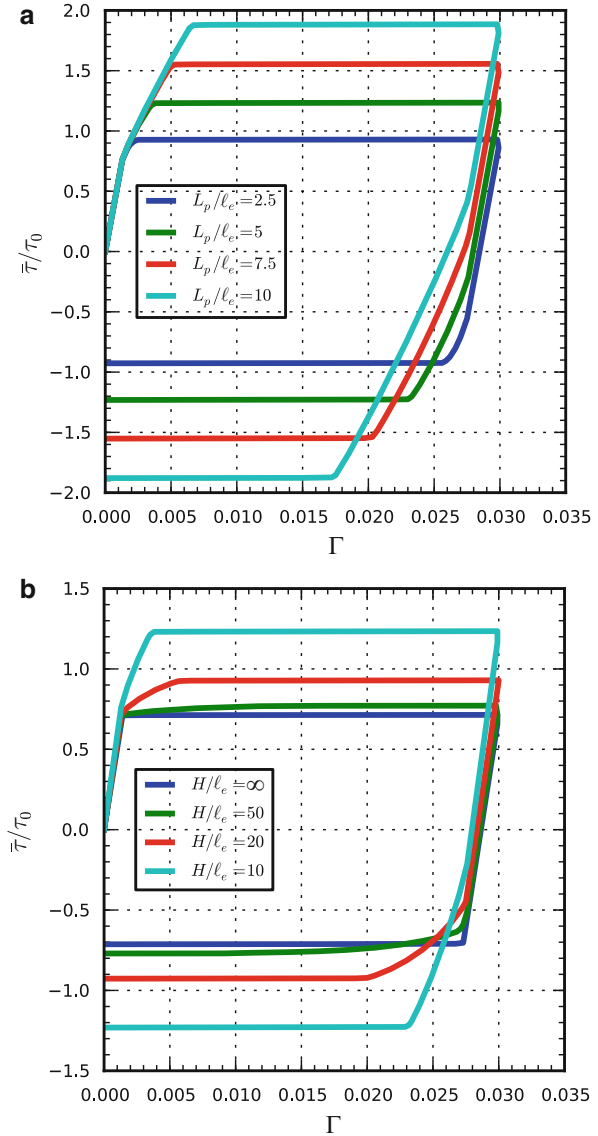
and Limkumnerd and van der Giessen (2008). A more detailed exposition of the
micropolar results are contained in Mayeur and McDowell (2013). The specimen
geometry is film oriented for symmetric slip with thickness, H, in the x_2-direction
as shown in Fig. 2. The slip systems are oriented at $\pm 30°$ with respect to the
x_2-direction. The top and bottom surfaces are modeled as rigid dislocation barriers
(impenetrable), the bottom surface is fully constrained against displacement, and
a uniform horizontal displacement is applied to the top surface while the vertical

Table 1 Summary of constitutive model parameters used in the micropolar single crystal simulations

Parameter	Symbol		Magnitude			Unit
–	–	Constrained shear	Bending SS	Bending DS	Composite	–
Shear modulus	μ	26.3	26.3	26.3	26.3	GPa
Poisson's ratio	ν	0.33	0.33	0.33	0.33	–
Couple modulus	μ_c	263	263	263	263	GPa
Elastic length scale	ℓ_e	10, 15	125, 125	300, 600	125	nm
Plastic length scale	$L_\perp$	45	562.5, 250	750, 700	125	nm
Reference threshold stress	r_0	12.78	10	10	13, 21, 30	MPa
Threshold stress coefficient	c_1	0.5	N/A	0.5	N/A	–
Burgers vector magnitude	b	0.25	0.25	0.25		nm
Hardening matrix coefficients	$h^{\alpha\beta}$	$\delta^{\alpha\beta}$	N/A	1.0	N/A	–
Initial SSD density	ϱ_{S0}	10^{-6}	N/A	10^{-6}	N/A	μm^{-2}
Dislocation interaction coefficients	$a^{\alpha\beta}$	$\delta^{\alpha\beta}$	N/A	1.0	N/A	–
Dislocation segment length constant	K	16.67,18.18	N/A	160, 26	N/A	–
Dislocation capture radius	y_c	0	N/A	1.5	N/A	nm
Reference deformation rate	$\dot{\lambda}_0$	10^{-3}	10^{-3}	10^{-3}	10^{-3}	s^{-1}
Drag stress	g	5	5	5	5	MPa
Inverse rate sensitivity exponent	m	20	20	20	20	–

displacement is constrained. The load is applied under displacement control up to an average strain of $\Gamma = 0.03$. The discrete dislocation problem was modeled as a unit cell of width, W, and thickness, H, and was spatially discretized with uniformly sized quadrilateral finite elements with an element size of $h_e = W/30$. The material was modeled as having zero initial dislocation density and the sources were distributed randomly throughout the spatial domain. Individual dislocation source strengths
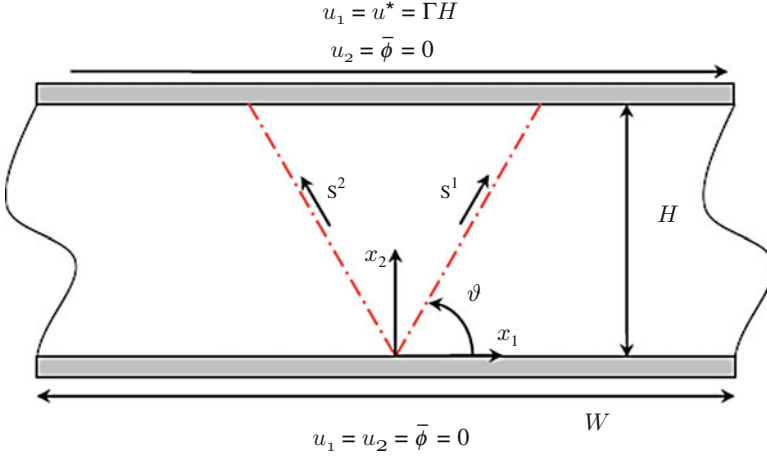
Fig. 2 Geometry schematic and boundary conditions for the constrained shear initial-boundary value problem

were determined by randomly sampling from a Gaussian distribution with a mean nucleation strength, $\overline{\tau}_{nuc} = 50$ MPa, and a standard deviation of $0.2\overline{\tau}_{nuc}$.

The displacement boundary conditions were applied at the top surface consistent with a constant strain rate of 10^3 s^{-1}. The constitutive parameters used in the simulations are representative of an aluminum single crystal.

$$
\begin{aligned}
&u_1\left(x_1, 0, t\right) = u_2\left(x_1, 0, t\right) = \overline{\phi}\left(x_1, 0, t\right) = 0 \\
&u_1\left(x_1, H, t\right) = \Gamma\left(x_1, H, t\right) H, \quad u_2\left(x_1, H, t\right) = \overline{\phi}\left(x_1, H, t\right) = 0 \\
&u_1\left(\tfrac{W}{2}, x_2, t\right) = u_1\left(-\tfrac{W}{2}, x_2, t\right), \quad u_2\left(\tfrac{W}{2}, x_2, t\right) = u_2\left(-\tfrac{W}{2}, x_2, t\right) \\
&\overline{\phi}\left(\tfrac{W}{2}, x_2, t\right) = \overline{\phi}\left(-\tfrac{W}{2}, x_2, t\right)
\end{aligned}
\tag{110}
$$

We only used the data for the 1 μm thick film in the calibration process since this is the only thickness for which all relevant deformation fields have been reported. Consistent with earlier nonlocal single crystal plasticity simulations of this problem, the isotropic hardening response is assumed to be linear (Shu et al. 2001; Bittencourt et al. 2003). Due to the symmetry of the problem and since it is impossible to differentiate between self and latent hardening effects from the available DDD results, we assume that $h^{\alpha\beta} = a^{\alpha\beta} = \delta^{\alpha\beta}$. Results are presented for two sets of constitutive parameters. As shown in Fig. 3, the stress-strain curves are nearly identical for both fits and are in good agreement with the discrete dislocation results. Fit 1 uses slightly more threshold hardening ($K_1 = 16.67$ vs. $K_2 = 18.18$), whereas fit 2 has a larger contribution from gradient kinematic hardening ($\ell_{e2} = 15$ nm vs. $\ell_{e1} = 10$ nm). The differences in the relative proportions of isotropic versus gradient kinematic hardening are evident in the shear strain distributions shown in Fig. 4. The profiles for fit 1 have a blunted shape as compared to the rounded morphology observed for

Fig. 3 Comparison of the average shear stress-strain response for $H = 1 \ \mu m$. Results for two parameter sets are shown to illustrate how differences in the local fields can vary for an identical average response. The discrete dislocation results are from Shu et al. (2001) and are given by the solid black line
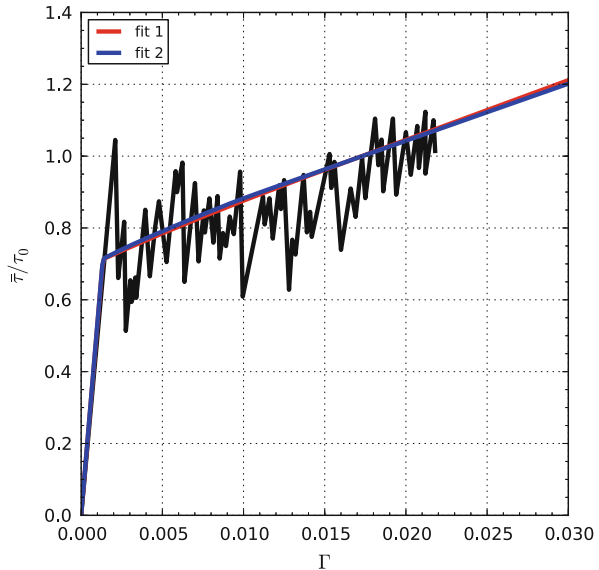
fit 2, which is consistent with the general observation that larger elastic length scales result in parabolic shear strain distributions. The signed GND density distributions for both fits are shown in Fig. 5a. The maximum GND densities at the boundary are marginally overpredicted and display steeper gradients in the near boundary regions than the discrete dislocation results, but compare favorably overall.

Pure Bending of Thin Films: Single Slip

The discrete dislocation results of the single slip bending configuration presented in this section were obtained by Yefimov et al. (2004b) and the micropolar results were given by Mayeur and McDowell (2011). The initial-boundary value problem is a thin film of width, W, and thickness, H, subjected to pure bending in a state of plane strain as sketched in Fig. 6. Considering a coordinate system attached to the midpoint of the film, the deformation is defined by the edge rotation angle, Θ, and is prescribed through a linear variation of the x_1 displacement component as a function of distance from the neutral axis:

$$u_1 \left(\pm \frac{W}{2}, x_2, t \right) = \pm \Theta(t) x_2. \tag{111}$$

The displacements are applied consistent with a constant average rotation rate, $10^{-3} \ \mathrm{s}^{-1}$, until a final rotation angle of $\Theta = 0.02$ is reached. The top and bottom surfaces of the beam are traction-free. As shown in Fig. 6, a single slip system is oriented at an angle ϑ with respect to the x_1-axis, and slip is constrained to occur

Fig. 4 Comparison of shear
strain distributions at
different levels of applied
strain for $H = 1$ μm: (**a**) fit 1
and (**b**) fit 2. The discrete
dislocation results are from
Shu et al. (2001) and are
given by the dashed lines
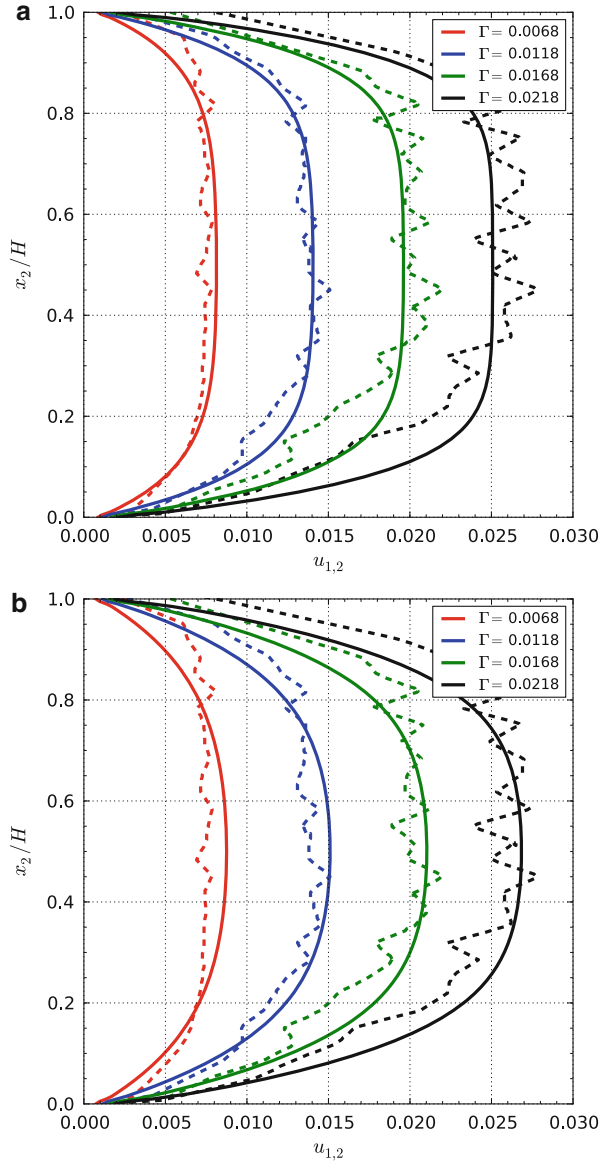
within region demarcated by the internal solid black lines. This restriction has been
imposed in the discrete dislocation simulations in order to avoid the complication of
having dislocations exit the crystal through the lateral faces where the displacement
boundary conditions are prescribed. Two different film thicknesses are considered
for the single slip configuration, $H = 2$ and 4 μm, respectively, with a fixed width-
to-thickness ratio of $W/H = 3$. Slip system orientations of 30° and 60° are studied
and will be referred to using the shorthand notation ϑ_{30} and ϑ_{60} in the following.

Fig. 5 Comparison of discrete dislocation and micropolar crystal plasticity dislocation density distributions at $\Gamma = 0.0168$ for $H = 1$ μm: (**a**) signed GND density and (**b**) SSD density. The discrete dislocation result is from Shu et al. (2001) and are given by the solid black line
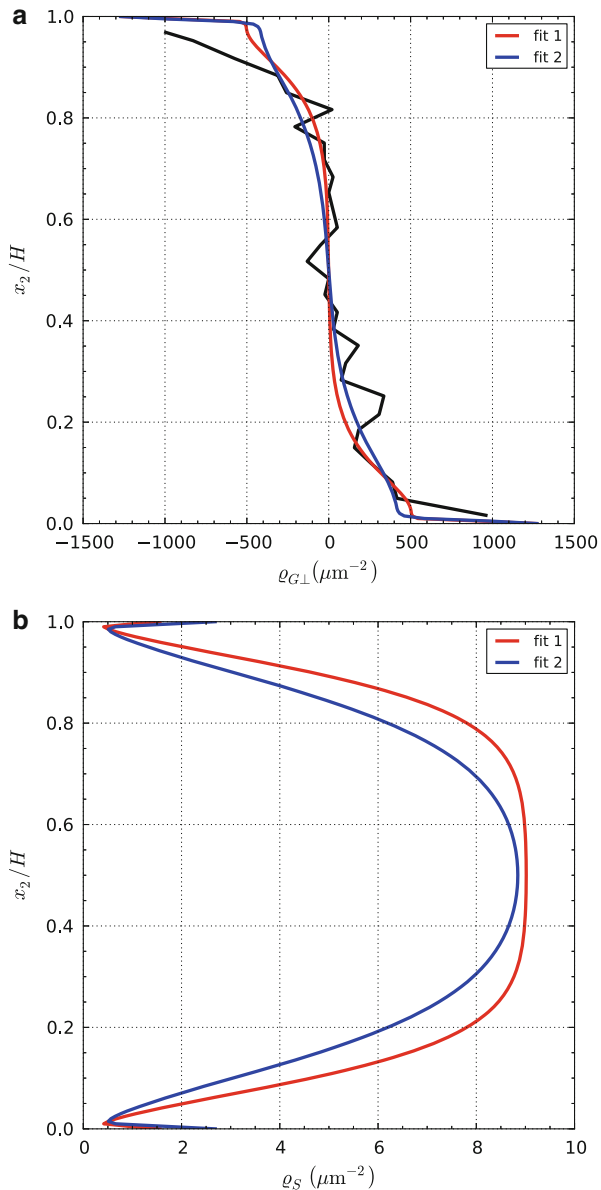
The average loading response is quantified by the bending moment, M, work-conjugate to Θ which is given by

$$M = \int_{-H/2}^{H/2} \sigma_{11}\left(\pm\frac{W}{2}, x_2\right) x_2 \, dx_2. \tag{112}$$
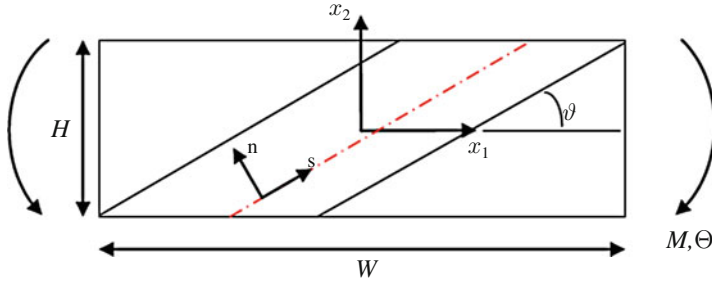
Fig. 6 Schematic of the geometry and slip system configuration for the single slip bending initial-boundary value problem

A thickness-independent measure of the average loading response is given by the normalized bending moment, M/M_{ref}, with the reference bending moment defined as: $M_{ref} = \frac{2}{3}\overline{\tau}_{nuc}\left(\frac{H}{2}\right)^2$. M_{ref} corresponds to the moment calculated from an assumed linear stress distribution over height of the beam with peak values of $\pm\overline{\tau}_{nuc}$ at the free surfaces. The mean critical nucleation stress, $\overline{\tau}_{nuc}$, is taken as 50 MPa in the discrete dislocation simulations. The micropolar finite element meshes, consistent with the DDD simulations, employ a uniform grid of bilinear quadrilaterals: 66×38 for ϑ_{30} and 155×30 for ϑ_{60}.

The normalized moment-rotation plots for both slip system orientations and thicknesses are plotted in Fig. 7, and they are in reasonably good agreement with the discrete dislocation results with respect to both the orientation and scale-dependence. Except for the 2 μm thick film for ϑ_{30}, the results are in good quantitative agreement with the initial yield strengths and nominal hardening rates predicted by the discrete dislocation model. The DDD results show that the yield strength for the 2 μm thick film for ϑ_{30} is lower than that of the 4 μm film in contradiction to an expected "smaller is stronger" trend, which underscores the stochastic nature of the initial flow stress obtained from DDD simulations. The discrete simulations display an approximately linear hardening rate that increases with decreasing film thickness, and the micropolar model shows similar trends although the rate is somewhat underestimated for the 2 μm thick film with ϑ_{60}. There is a substantially higher hardening rate for ϑ_{30} as compared to ϑ_{60} as shown in Fig. 7; this difference is primarily due to the way the boundary value problem is constructed with distinct elastic and plastic zones and is not a consequence of the local hardening behavior. Recall that the films are modeled as composite elastic-plastic materials with plastic deformation restricted to the interior region bounded by the solid lines parallel to the slip direction (see Fig. 6) for the sake of convenience in the DDD simulations. Therefore, the plastic zone size for ϑ_{30} is much smaller. The significantly higher apparent hardening rates for ϑ_{30} as compared to ϑ_{60} are essentially due to an increased volume fraction of the elastic phase and not dislocation hardening. In fact, a local crystal plasticity model with an elastic-perfectly plastic slip system level response would yield an apparent hardening

Fig. 7 Comparison of the discrete dislocation (DD) and micropolar crystal plasticity (MP) normalized moment-rotation response for the single slip bending configuration (**a**) $\vartheta = 30°$ and (**b**) $\vartheta = 60°$. The discrete dislocation results are from Yefimov et al. (2004b)
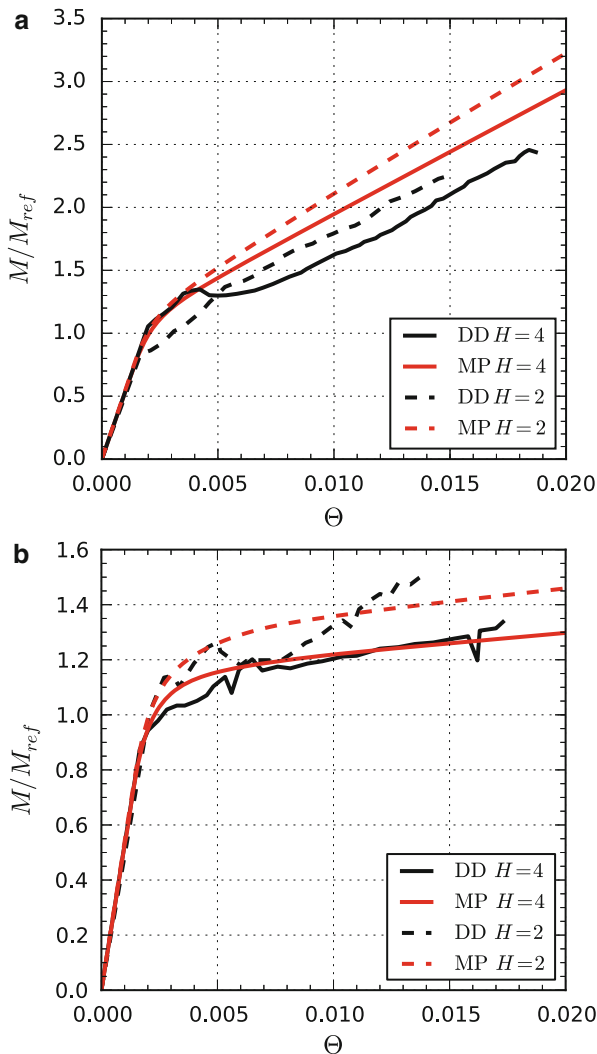
rate comparable to, albeit lower than that shown in Fig. 7a. Of course, there is a component of the apparent hardening rate differences for the two orientations due to the relative misalignment of the slip and axial strain directions, and this is the portion associated with variations in GND distributions between the two cases.

Dislocation density contour plots for both film thicknesses are shown in Figs. 8 and 9 for ϑ_{30} and ϑ_{60}, respectively, with $\Theta = 0.015$. In the ϑ_{30} film, the maximum dislocation densities are 39.8 μm^{-2} and 22.6 μm^{-2}, respectively, for 2 and 4 μm thick films. Dislocation-free zones are clearly observed along the neutral axis for both film thicknesses, where the thickness of the dislocation-free region is approximately 3–4 times larger for the 4 μm thick film. As compared to the
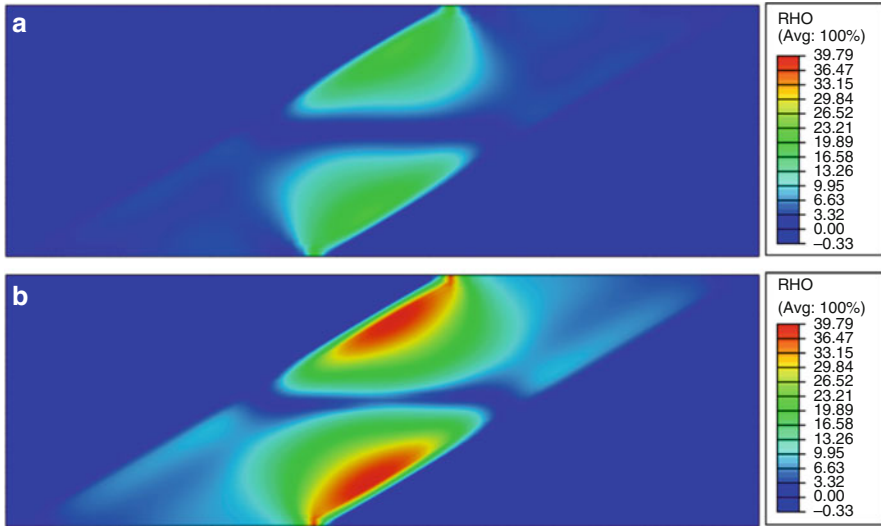
Fig. 8 Dislocation density distributions predicted by the micropolar crystal plasticity simulations at $\Theta = 0.015$ for $\vartheta = 30°$: (**a**) $H = 4\ \mu\text{m}$ (**b**) $H = 2\ \mu\text{m}$
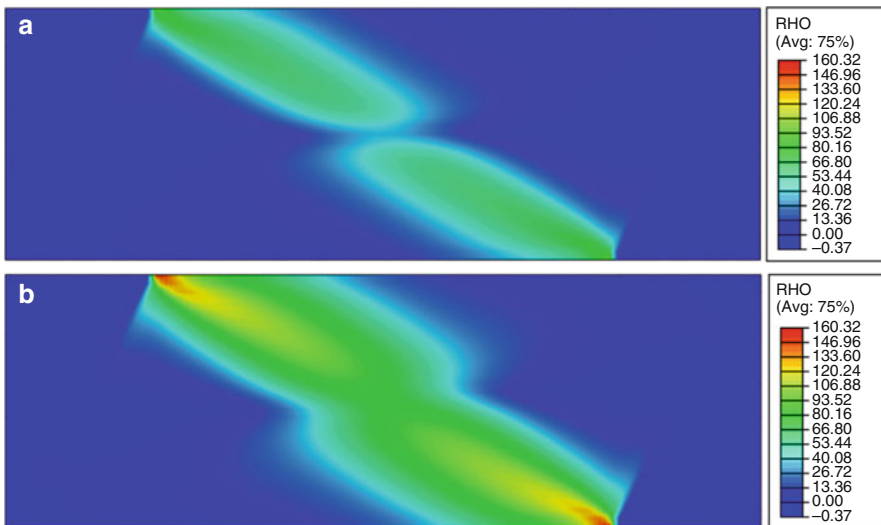
Fig. 9 Dislocation density distributions predicted by the micropolar crystal plasticity simulations at $\Theta = 0.015$ for $\vartheta = 60°$: (**a**) $H = 4\ \mu\text{m}$ (**b**) $H = 2\ \mu\text{m}$

ϑ_{30} film, the dislocation density distributions for ϑ_{60} are markedly different. The morphology of the distribution can be characterized as having ellipsoidal-shaped lobes originating at the free surface near the corner of the elastic-plastic interface and extending perpendicular to elastic-plastic interface toward the neutral axis. The

Fig. 10 Comparison of the discrete dislocation (DD) and micropolar crystal plasticity (MP) dislocation density evolution as a function of average plastic curvature for both orientations of the single slip configuration. The dashed curves are for ϑ_{60}. The discrete dislocation results are from Yefimov et al. (2004b)
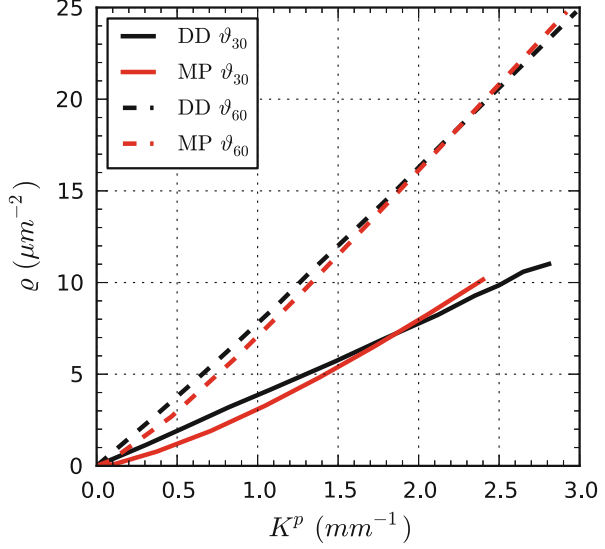
maximum local dislocation densities, 160 μm^{-2} ($H = 2$ μm) and 98.3 μm^{-2} ($H = 4$ μm), are significantly higher than in the v_{30} film. The contour plots exhibit rather high dislocation density at the free surfaces that are generated in response to the strong rotational gradients that arise due to the compliance mismatch at the elastic-plastic interface. This is in contrast to the DDD simulations which exhibit dislocation-free zones at the free surfaces that are thought to be the result of an image force effect. It is possible that an image force effect might be imposed within the micropolar framework through an appropriately specified higher-order traction along the free surfaces; however, this avenue has yet to be pursued.

In Fig. 10, the total dislocation density computed over the entire volume is plotted as a function of the imposed deformation for both orientations with $H = 4$ μm. It is shown that the micropolar model accurately captures the evolution as predicted by the DDD simulations. The dislocation density is computed by volume averaging the centroidal element values over the FE mesh, and the average plastic curvature, K^p, is calculated according to

$$K^p = \frac{2\Theta}{W} - \frac{M}{EI}. \tag{113}$$

Here, EI is the in-plane bending stiffness defining the elastic curvature. The total GND density required to accommodate an imposed bending angle, Θ, can be calculated according to Ashby (1970) in terms of K^p as

$$\hat{\rho} = \frac{K^p}{b_1}, \tag{114}$$

where b_1 is the magnitude of the x_1-component of the Burgers vector. The plot shows that the dislocation density increases in an approximately linear fashion with respect to the plastic curvature for both sets of simulations. Also, as expected from Eq. (114), the dislocation density at a given level of plastic curvature is higher for the ϑ_{60} film. Since the x_1-component of the Burgers vector is smaller for this orientation, more dislocations are needed to accommodate the imposed strain gradient.

Pure Bending of Thin Films: Double Slip

Next we study pure bending of thin films with a double slip system configuration as shown in Fig. 11. The DDD simulation results presented were originally reported by Yefimov and van der Giessen (2005a) and an analysis using micropolar crystal plasticity was presented by Mayeur (2010). As in the single slip case, two orientations are considered, ϑ_{30} and ϑ_{60} where the orientation angle is also defined as the angle between the x_1-axis and the slip direction for slip system 1. For each orientation, the second slip system is symmetrically aligned with respect to the x_2-axis. The films are partitioned into elastic and plastic phases as before and in accordance with the discrete dislocation simulations. The elastic zones are the triangular regions located at the top, bottom, left, and right ends of the film as shown in Fig. 11, and each slip system is only active in the slice of material parallel to the slip direction. Thus, the plastic zone can be divided into five regions: four single slip regions (two for each slip system) that are the outermost diagonal regions and a diamond-shaped double slip region located at the center of the film and is demarcated by the blue dotted lines in the schematic. The boundary conditions and FE discretizations are the same as for the single slip configuration. Simulations are carried out for film thicknesses of 4 μm and 8 μm with fixed aspect ratio $W/H = 3$.

The normalized moment-rotation responses for both film thicknesses and orientations are plotted in Fig. 12 against the discrete dislocation results, and the results compare favorably. The response is similar for both orientations unlike the single slip configuration, where the hardening rate was much higher for the ϑ_{30} films due
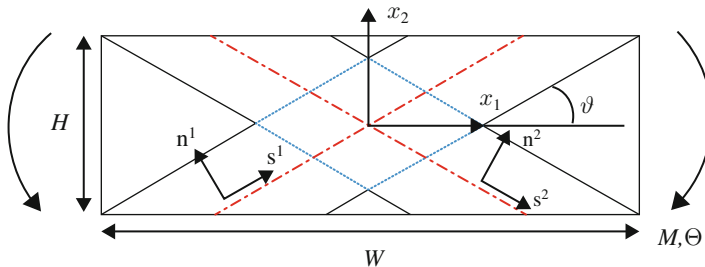

Fig. 11 Schematic of the geometry and slip system configuration for the double slip bending initial-boundary value problem

Fig. 12 Comparison of the discrete dislocation (DD) and micropolar crystal plasticity (MP) normalized moment-rotation response for the double slip bending configuration (**a**) $\vartheta = 30°$ and (**b**) $\vartheta = 60°$. The discrete dislocation results are from Yefimov and van der Giessen (2005a)
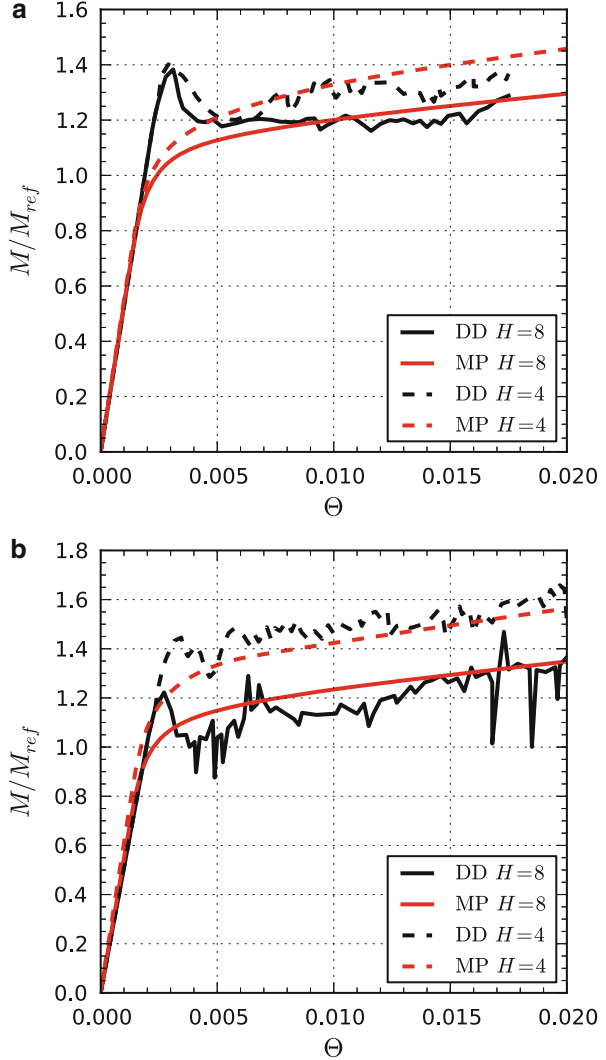
to larger effective film thickness resulting from the dominant influence of the elastic regions. However, the behavior for the ϑ_{60} films has a stronger scale-dependence as would be expected given that more GNDs are necessary to accommodate the strain gradients for the ϑ_{60} film. In contrast to the single slip simulations, we found that different elastic length scales and dislocation multiplication constants, K, are required for each orientation to obtain a good match with the DDD results.

Figure 13 shows the total dislocation density contour plots for the ϑ_{30} films at $\Theta = 0.02$, and we note that the magnitude of the total dislocation density field is approximately three orders of magnitude larger than that of the SSD density field
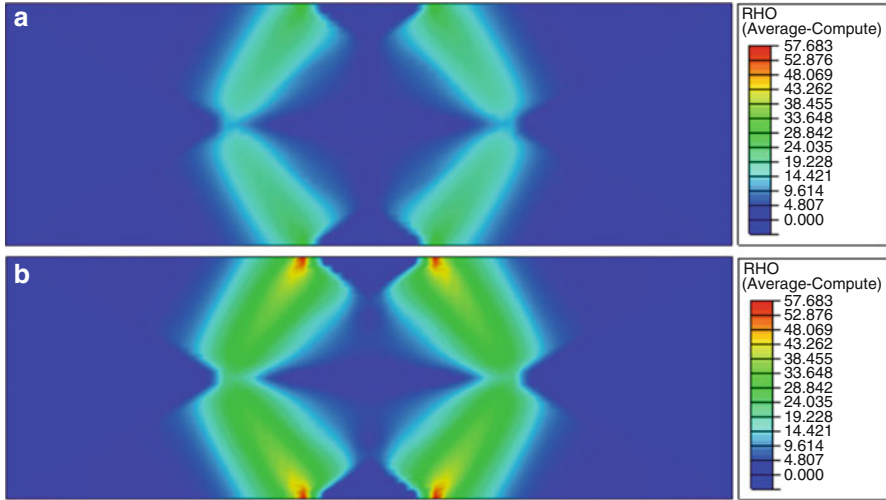
Fig. 13 Dislocation density distributions predicted by the micropolar crystal plasticity simulations at $\Theta = 0.02$ for $\vartheta = 30°$: (**a**) $H = 8 \ \mu$m (**b**) $H = 4 \ \mu$m

(not shown), which is characteristic of confined micro-scale dislocation plasticity. The maximum dislocation density is located at the free surfaces near the elastic-plastic interfaces for both film thicknesses, with peak values of 57.7 μm^{-2} and 32.3 μm^{-2} for the 4 μm and 8 μm thick films, respectively. In the case of the 8 μm thick film, there is dislocation-limited region (not dislocation-free) adjacent to the neutral axis separating the regions of higher dislocation density, whereas the dislocation distributions are continuous across the neutral axis for the 4 μm thick film. This is in contrast to the dislocation density fields for the single slip configuration (see Fig. 8) which exhibit a clear dislocation starved zone adjacent to the neutral axis. It is interesting that the maximum dislocation density values occur in the single slip regions and that the double slip region has a significantly lower density.

Figure 14 shows the total dislocation density contour plots for the ϑ_{60} films at $\Theta = 0.02$. The geometrical configuration of the elastic and plastic phases for the ϑ_{60} oriented crystal is such that there is no centrally located elastic zone and the majority of the plastic phase is a double slip region. Therefore, the dislocation density fields are continuous and smooth, in contrast to the ϑ_{30} orientation where the dislocation density field has a checkered type of pattern. The local maximum in the dislocation density fields are comparable for both orientations, thus the total (over the entire plastic region) dislocation density is much higher for the ϑ_{60} film.

The total film dislocation density is plotted for both slip orientations and thicknesses versus the average plastic curvature in Fig. 15. In general, the micropolar results compare favorably to the discrete dislocation results. The micropolar model captures the change in slope of the dislocation density-plastic curvature plot with
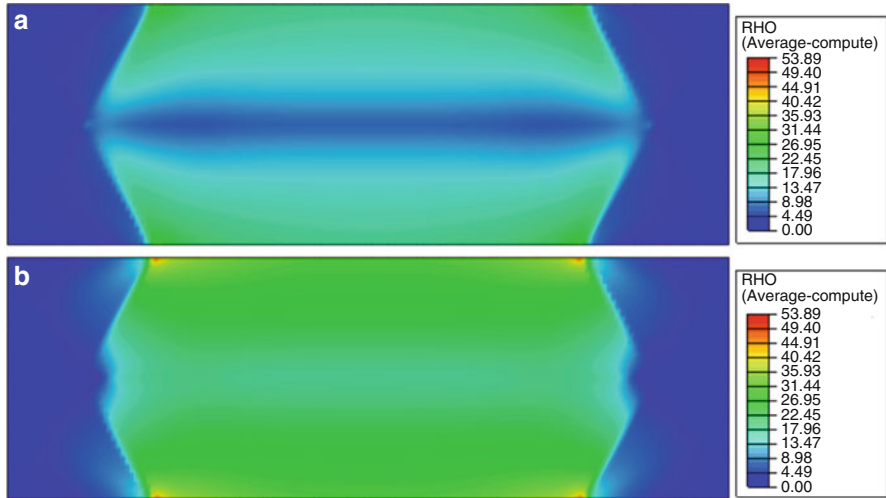
Fig. 14 Dislocation density distributions predicted by the micropolar crystal plasticity simulations at $\Theta = 0.02$ for $\vartheta = 60°$: (**a**) $H = 8\,\mu\text{m}$ (**b**) $H = 4\,\mu\text{m}$

the change in thickness for the ϑ_{30} oriented films, but not for the ϑ_{60} oriented films. An increase in the slope is predicted for the ϑ_{30} films but the micropolar results are nearly identical for the ϑ_{60} films. The DDD results for the 8 μm thick film show an increase in slope with increasing average plastic curvature, while the slope for the 4 μm remains essentially constant.

Simple Shear of a Metal Matrix Composite

In this application we study the size-dependent hardening of a metal matrix composite subjected to simple shear. The idealized particle reinforced system shown in Fig. 16 was previously analyzed using DDD simulations by Cleveringa et al. (1997, 1999) and Yefimov et al. (2004a) and micropolar crystal plasticity by Mayeur and McDowell (2015). The periodic unit cell consists of an elastic-viscoplastic matrix phase (white) with a single slip system parallel to the x_1 direction, reinforced by elastic particles (gray). The size of the unit cell is $2W \times 2H \left(W = H\sqrt{3} \right)$ and the particles have dimensions $2W_f \times 2H_f$. Two distinct cases, denoted Material I and Material II, with different particle aspect ratios but the same area fraction, $A_f = (H_f W_f)/(HW) = 0.2$, are studied: the unit cell for Material I is reinforced by square particles with $W_f = H_f = 0.416H$, while the unit cell for Material II is reinforced by rectangular particles with $H_f = 2W_f = 0.588H$. The two cases are differentiated such that Material I contains an unobstructed vein of matrix material that spans the unit cell, whereas the particles overlap in Material II and block slip. Since the area fraction of the elastic particles is the same for both morphologies,

Fig. 15 Comparison of the discrete dislocation (DD) and micropolar crystal plasticity (MP) dislocation density evolution as a function of average plastic curvature for the double slip configuration (**a**) $H = 4\ \mu$m and (**b**) $H = 8\ \mu$m. The discrete dislocation results are from Yefimov and van der Giessen (2005a)
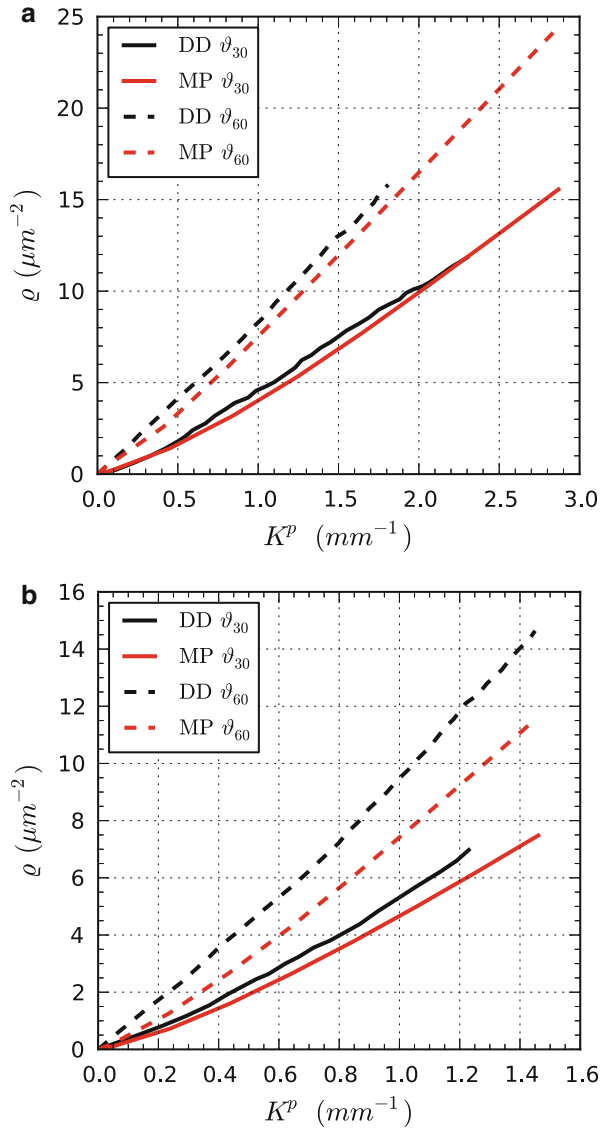
any observed differences in material response are due to the dislocation-particle interactions and not the phase volume fraction.

The composite is subjected to simple shear through displacement boundary conditions applied to top and bottom surfaces and these surfaces are assumed to be couple stress traction free. Periodic boundary conditions are enforced on displacements and microrotation at the left and right surfaces. The deformation is imposed at a shearing rate of $\dot{\Gamma} = 10^{-3}\mathrm{s}^{-1}$ up to a unit cell shear strain of $\Gamma = 0.01$,
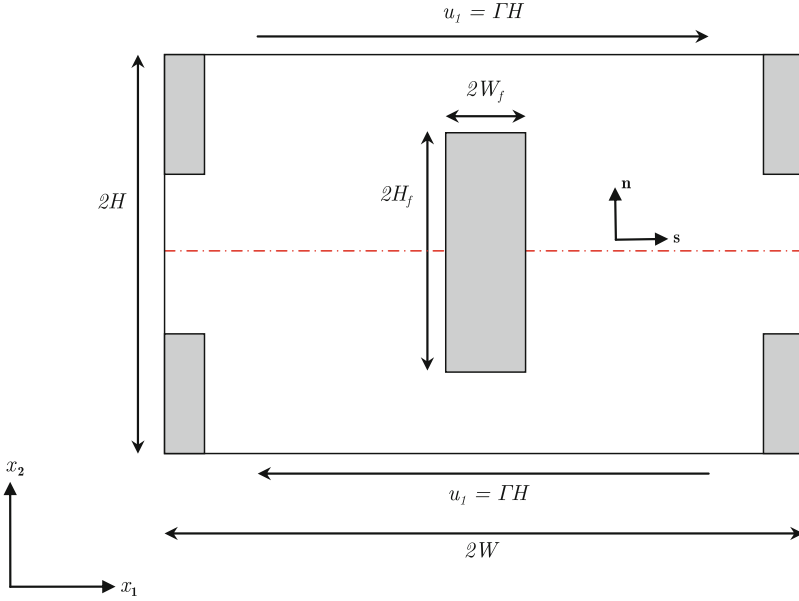
Fig. 16 Schematic of the geometry and slip system configuration for the metal matrix composite initial-boundary value problem

at which point the material is unloaded back to zero strain. The boundary conditions are stated as:

$$u_1(x_1, \pm H, t) = \pm \Gamma(t)H, \quad u_2(x_1, \pm H, t) = 0$$
$$u_1(-W, x_2, t) = u_1(W, x_2, t), \quad u_2(-W, x_2, t) = u_2(W, x_2, t) \quad (115)$$
$$\overline{\phi}(-W, x_2, t) = \overline{\phi}(W, x_2, t).$$

Further, microrotation is assumed to be coupled at the matrix-particle interface. Simulations are performed for cell sizes of $H = \{0.5C, C, 2C\}$ where $C = 4000b$ with $b = 0.25$ nm. The FE mesh consists of 106×61 bilinear quadrilateral elements. The classical elastic properties of the particles are $\mu = 192.3$ GPa and $\nu = 0.17$, and the matrix constitutive parameters are listed in Table 1. These parameters are representative of silicon carbide particles embedded in an aluminum matrix. With regard to specifying the nonclassical elastic constants for inclusion, μ_c^I and β^I, we assume that $\mu_I^c = \mu_M^c$ and $\beta^I = \beta^M$ where the superscripts I and M refer to the inclusion and matrix, respectively. As discussed by Cordero et al. (2010), other choices are possible and perhaps should be considered in future work.

As shown in Fig. 17a, the unit-cell average stress-strain response predicted by the discrete dislocation model for Material I is nearly elastic-perfectly plastic, whereas Material II displays an approximately linear hardening rate. Material I does not harden because there are no obstacles to dislocation motion. In contrast, mobile

Fig. 17 Average stress-strain response for (**a**) Material I and II for $H = C$ and (**b**) Material II with variable slip threshold for different particle spacings. Dashed lines are discrete dislocation results (Yefimov, 2004a) and solid lines are micropolar results
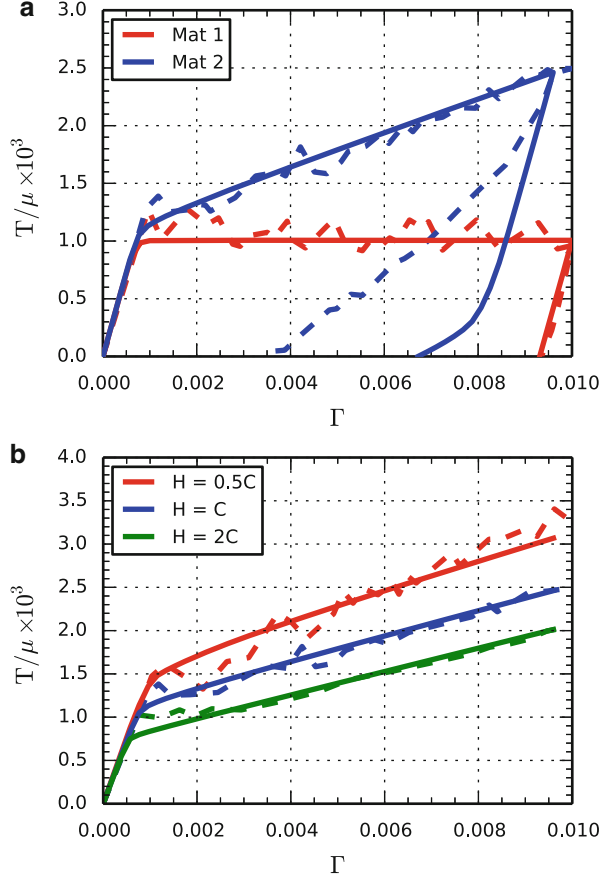
dislocations in Material II are obstructed by the particles and form pileups and tilt walls at the matrix-particle interface. The unloading curve suggests the material strengthening in Material II is governed by the development of a strong back stress, as evidenced by the pronounced Bauschinger effect, while unloading is essentially elastic for Material I. The average stress-strain curves predicted by the micropolar model (solid lines in Fig. 17) are in good agreement with the discrete dislocation results during forward loading; however, the Bauschinger effect for Material II is significantly underestimated. Figure 17b shows the stress-strain curves for Material II for the three unit cell sizes. We found that it was necessary to use different r_0 values to obtain good agreement with the discrete dislocation results. Interestingly, the calibrated values, $r_0 = \{13, 21, 30\}$ MPa, show strong correlation with the Hall-Petch relation $r_0 \propto \Lambda^{-1/2}$, where $\Lambda = \left(2\sqrt{3} - 0.588\right) H$ is the mean free path for Material II. The slope of the Hall-Petch relation is 40.51 MPa $\sqrt{\mu m}$. Note that the Hall-Petch relation was not assumed a priori, but rather is consistent with the result of parameter estimation.

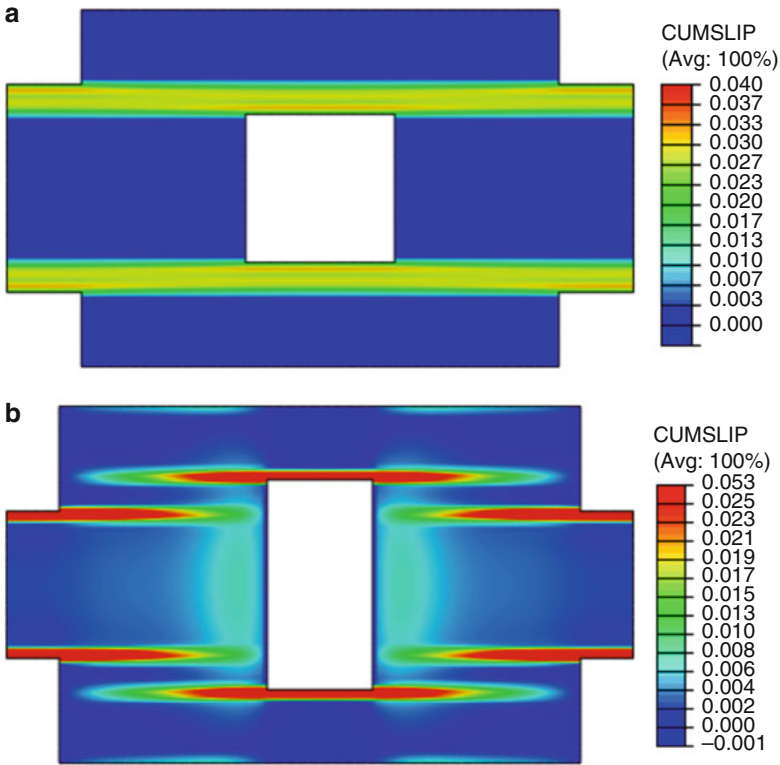**Fig. 18** Contours of cumulative slip at $\Gamma = 0.006$ for (**a**) Material I (**b**) Material II ($H = C$)

The cumulative plastic slip distributions for both cases with $H = C$ and $\Gamma = 0.006$ as predicted by the micropolar model are shown in Fig. 18. The slip field morphology for Material I is characterized by intensely localized plasticity in the unreinforced veins of matrix material, whereas the slip morphology for Material II is characterized by highly localized bands that form along the top and bottom faces of the particles, but do not extend across the full width of the unit cell due the particle overlap. The cumulative slip distributions predicted by the micropolar model are consistent with the discrete dislocation simulations and are noticeably different than the predictions of local and low-order gradient theories, which show much higher levels of slip accumulation along the vertical matrix-particle interfaces.

The total dislocation density fields are plotted for all three cases of Material II in Fig. 19 at $\Gamma = 0.006$. There is a significant dislocation density accumulation along the vertical faces of the matrix-particle interface and sparse dislocation density distributed throughout the matrix. These GNDs are generated to accommodate the rotational gradients that develop at the interface (Ashby 1970). The total matrix dislocation density is plotted during loading as a function of applied shear strain for both the micropolar and discrete dislocation models for the three unit cell sizes in
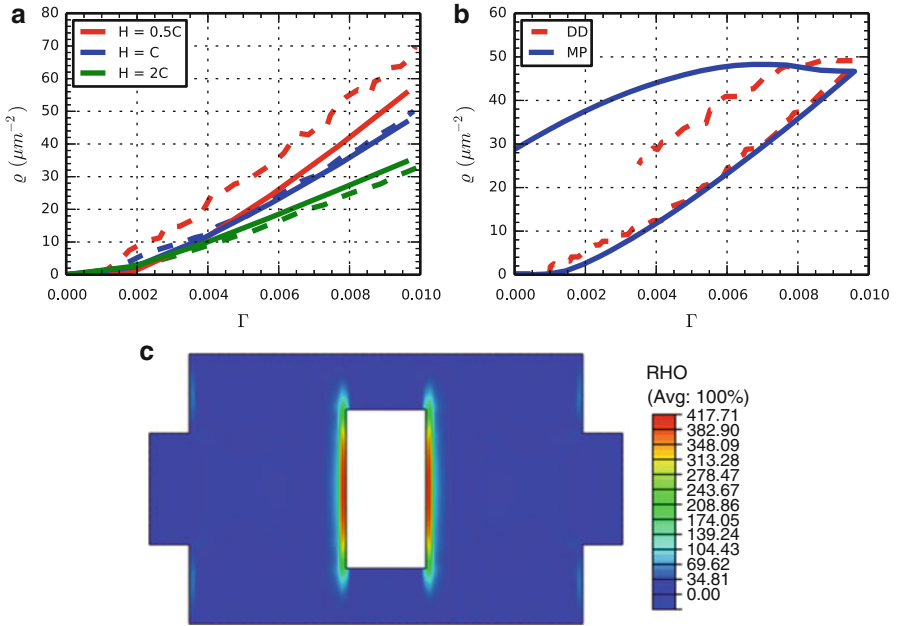
Fig. 19 Evolution of total matrix dislocation density versus applied strain as predicted by the micropolar model (solid lines) and discrete dislocation dynamics (dashed lines) (Yefimov et al. 2004a) (**a**) for various unit cell sizes during loading and (**b**) unloading for $H = C$. Contour of total dislocation density for Material II at $\Gamma = 0.006$ for the micropolar model $H = 0.5C$

Fig. 19a and during loading/unloading for $H = C$ in Fig. 19b. The micropolar results are in good agreement with the discrete dislocation simulations for the two largest unit cells during loading, but there is a modest departure in the model predictions for the $H = 0.5C$ case. Interestingly, the discrete dislocation model predicts much higher rate of dislocation recovery upon unloading as compared to the micropolar model.

Overall, the predictions of the micropolar simulations are in reasonably good agreement with the discrete dislocation simulation results. The most significant discrepancy in the simulated material response is the underprediction of the Bauschinger effect and the rate of dislocation recovery upon unloading. We believe these discrepancies are largely related to the higher-order boundary conditions enforced at the matrix-particle interface. It is assumed that the lattice rotations at the matrix-particle interface are equal in these simulations, i.e., the finite element nodes along the matrix-particle interface are shared between the two materials. This represents a different boundary condition than what is enforced at the matrix-particle interface in the discrete dislocation simulation. The interface boundary condition enforced in the DDD models is one of equal displacements and zero slip at the vertical matrix-particle faces. Thus, the micropolar model enforces an additional constraint at the matrix-particle interface, which may overconstrain the material

response upon unloading. It may be possible to achieve an improved unloading response by either modifying boundary conditions at the matrix-particle interface or the nonclassical elastic constants of the inclusion, μ_c^I and β^I, which will alter the way higher-order tractions are transmitted between the two phases.

Conclusions

Micropolar crystal plasticity is a specialized subset of the more general micromorphic crystal plasticity theory, discussed in a subsequent chapter, that accounts for size effects due to gradients of lattice rotation. The connection between the micropolar lattice torsion-curvature and Nye's GND tensor was established and related to concepts from slip gradient-based crystal plasticity. The advantage of the micropolar theory in comparison to the micromorphic and slip gradient-based theories is the reduced complexity in that it requires only three additional continuum degrees of freedom for the fully three-dimensional case.

A full treatment of the finite deformation kinematics and thermodynamic-based constitutive equations have been developed and placed in context as an extension of concepts of local crystal plasticity theory. A model employing linearized kinematics is then presented with an explicit set of constitutive equations that were used in finite element simulations of initial-boundary value problems previously solved using discrete dislocation dynamics (DDD). The simulation results demonstrate the ability of the micropolar theory to capture many of the salient features exhibited by the DDD simulations for a wide range of boundary value problems, including both the size-dependence of the stress-strain response and the evolution of the dislocation density.

An extended comparison to Gurtin-type slip gradient-based theories of higher-order single crystal plasticity was presented. The analysis highlights many striking theoretical similarities, which suggests that they will also share many of the same predictive capabilities. A few subtle, but key differences, with respect to the construction of dissipative constitutive equations are also discussed. For example, it is possible in the slip gradient-based theories to isolate gradient energetic and dissipative length scale effects, whereas they are coupled in the micropolar theory, i.e., one cannot have gradient dissipative effects in the absence of energetic gradient effects since there will be no driving force for plastic torsion-curvature evolution. However, it is noted that there is no principal restriction preventing one from casting the micropolar theory in terms of energetic-dissipative decomposition of the couple stress tensor rather than of the lattice torsion-curvature, which would then accommodate a true separation of energetic and dissipative gradient effects.

There is still much exciting work to be done in further developing the micropolar theory. Two areas of particular interest are the development of proper intermediate higher-order boundary conditions between fully constrained (micro-hard) and traction free (micro-free) and the proper description of interface boundary conditions and/or constitutive equations for grain and/or phase boundaries.

References

Abaqus/Standard Version 6.7.1. Dassault Systèmes Simulia Corp. (2007)

E. Aifantis, On the microstructural origin of certain inelastic models. J. Eng. Mater. Technol. **106**, 326–330 (1984)

A. Arsenlis, D.M. Parks, Crystallographic aspects of geometrically-necessary and statistically-stored dislocation density. Acta Mater. **47**, 1597–1611 (1999)

M.F. Ashby, Deformation of plastically non-homogeneous materials. Philos. Mag. **21**(170), 399–424 (1970)

E. Bittencourt, A. Needleman, M.E. Gurtin, E. van der Giessen, A comparison of nonlocal continuum and discrete dislocation plasticity predictions. J. Mech. Phys. Solids **51**, 281–310 (2003)

P. Cermelli, M. Gurtin, On the characterization of geometrically necessary dislocations in finite plasticity. J. Mech. Phys. Solids **49**, 1539–1568 (2001)

J. Clayton, D. Bamman, D. McDowell, A geometric framework for the kinematics of crystals with defects. Philos. Mag. **85**, 3983–4010 (2005)

H.H.M. Cleveringa, E. van der Giessen, A. Needleman, Comparison of discrete dislocation and continuum plasticity predictions for a composite material. Acta Mater. **45**, 3163–3179 (1997)

H.H.M. Cleveringa, E. van der Giessen, A. Needleman, A discrete dislocation analysis of residual stresses in a composite material. Philos. Mag. A Phys. Condens. Matter Struct. Defects Mech Prop **79**, 893–920 (1999)

B.D. Coleman, M.E. Gurtin, Thermodynamics with internal state variables. J. Chem. Phys. **47**(2), 597–613 (1967)

N.M. Cordero, A. Gaubert, S. Forest, E.P. Busso, F. Gallerneau, S. Kruch, Size effects in generalised continuum crystal plasticity for two–phase laminates. J. Mech. Phys. Solids **58**, 1963–1994 (2010)

A. Eringen, *Microcontinuum Field Theories I: Foundations and Solids* (Springer, New York, 1999)

A.C. Eringen, W.D. Claus Jr., A micromorphic approach to dislocation theory and its relation to several existing theories. Technical Report TR-6, Princeton University Department of Aerospace and Mechanical Sciences (1969)

A.C. Eringen, E.S. Suhubi, Nonlinear theory of simple micro-elastic solids-I. Int. J. Eng. Sci. **2**, 189–203 (1964)

L.P. Evers, W.A.M. Brekelmans, M.G.D. Geers, Non-local crystal plasticity model with intrinsic SSD and GND effects. J. Mech. Phys. Solids **52**, 2379–2401 (2004)

S. Forest, Some links between Cosserat, strain gradient crystal plasticity and the statistical theory of dislocations. Philos. Mag. **88**, 3549–3563 (2008)

S. Forest, Generalized continuum modelling of crystal plasticity, in *Generalized Continua and Dislocation Theory* (Springer, Vienna, 2012), pp. 181–287

S. Forest, R. Sievert, Elastoviscoplastic constitutive frameworks for generalized continua. Acta Mech. **160**, 71–111 (2003)

S. Forest, G. Cailletaud, R.W. Sievert, A Cosserat theory for elastoviscoplastic single crystals at finite deformation. Arch. Mech. **49**, 705–736 (1997)

S. Forest, F. Barbe, G. Cailletaud, Cosserat modelling of size effects in the mechanical behaviour of polycrystals and multi-phase materials. Int. J. Solids Struct. **37**(46), 7105–7126 (2000)

P. Germain, The method of virtual power in continuum mechanics. Part 2: microstructure. SIAM J. Appl. Math. **25**, 556–575 (1973)

W. Günther, Zur Statik und Kinematik des Cosseratschen Kontinuums. Abh. Braunschw. Wiss. Ges. **10**, 195–213 (1958)

M.E. Gurtin, A gradient theory of single–crystal viscoplasticity that accounts for geometrically necessary dislocations. J. Mech. Phys. Solids **50**, 5–32 (2002)

M.E. Gurtin, L. Anand, S.P. Lele, Gradient single-crystal plasticity with free energy dependent on dislocation densities. J. Mech. Phys. Solids **55**, 1853–1878 (2007)

E. Kröner, On the physical reality of torque stresses in continuum mechanics. Int. J. Eng. Sci. **1**, 261–278 (1963)

E. Kröner, Initial studies of a plasticity theory based upon statistical mechanics, in *Inelastic Behaviour of Solids*, ed. by M. Kanninen, W. Adler, A. Rosenfield, R. Jaffee (McGraw-Hill, New York, 1969), pp. 137–147

M. Kuroda, V. Tvergaard, A finite deformation theory of higher-order gradient crystal plasticity. J. Mech. Phys. Solids **56**(8), 2573–2584 (2008)

S. Limkumnerd, E. van der Giessen, Study of size effects in thin films by means of a crystal plasticity theory based on DiFT. J. Mech. Phys. Solids **56**, 3304–3314 (2008)

J.R. Mayeur, Generalized continuum modeling of scale-dependent crystalline plasticity. Ph.D. thesis, Georgia Institute of Technology, 2010

J.R. Mayeur, D.L. McDowell, Bending of single crystal thin films modeled with micropolar crystal plasticity. Int. J. Eng. Sci. **49**, 1357–1366 (2011)

J.R. Mayeur, D.L. McDowell, An evaluation of higher-order single crystal strength models for constrained thin films subjected to simple shear. J. Mech. Phys. Solids **61**, 1935–1954 (2013)

J.R. Mayeur, D.L. McDowell, A comparison of Gurtin type and micropolar theories of generalized single crystal plasticity. Int. J. Plast. **57**, 29–51 (2014)

J.R. Mayeur, D.L. McDowell, Micropolar crystal plasticity simulation of particle strengthening. Model. Simul. Mater. Sci. Eng. **23**, 065007 (2015)

J.R. Mayeur, D.L. McDowell, D.J. Bammann, Dislocation-based micropolar single crystal plasticity: comparison of multi- and single criterion theories. J. Mech. Phys. Solids **59**, 398–422 (2011)

H. Mecking, U.F. Kocks, Kinetics of flow and strain-hardening. Acta Metall. **29**, 1865–1875 (1981)

J.F. Nye, Some geometrical relations in dislocated crystals. Acta Metall. **1**, 153–162 (1953)

B.D. Reddy, The role of dissipation and defect energy in variational formulations of problems in strain-gradient plasticity. Part 2: single-crystal plasticity. Contin. Mech. Thermodyn. **23**, 551–572 (2011)

H. Schäfer, Eine Feldtheorie der Versetzungen im Cosserat-Kontinuum. Z. Angew. Math. Phys. **20**, 891–899 (1969)

J.Y. Shu, N.A. Fleck, E. van der Giessen, A. Needleman, Boundary layers in constrained plastic flow: comparison of nonlocal and discrete dislocation plasticity. J. Mech. Phys. Solids **49**, 1361–1395 (2001)

R. Sievert, S. Forest, R. Trostel, Finite deformation Cosserat-type modelling of dissipative solids and its application to crystal plasticity. J. Phys. IV **8**, 357–364 (1998)

C. Teodosiu, F. Sidoroff, A theory of finite elastoviscoplasticity of single crystals. Int. J. Eng. Sci. **14**, 165–176 (1976)

S. Yefimov, E. van der Giessen, Multiple slip in a strain-gradient plasticity model motivated by a statistical-mechanics description of dislocations. Int. J. Solids Struct. **42**, 3375–3394 (2005a)

S. Yefimov, E. van der Giessen, Size effects in single crystal thin films: nonlocal crystal plasticity simulations. Eur. J. Mech. A Solids **24**, 183–193 (2005b)

S. Yefimov, I. Groma, E. van der Giessen, A comparison of a statistical-mechanics based plasticity model with discrete dislocation plasticity calculations. J. Mech. Phys. Solids **52**, 279–300 (2004a)

S. Yefimov, E. van der Giessen, I. Groma, Bending of a single crystal: discrete dislocation and nonlocal crystal plasticity simulations. Model. Simul. Mater. Sci. Eng. **12**, 1069 (2004b)